Phys Chem Minerals (2004) 31: 606–624
DOI 10.1007/s00269-004-0419-6

ORIGINAL PAPER

P. F. Schofield · K. S. Knight · J. A. M. van der Houwen
E. Valsami-Jones

The role of hydrogen bonding in the thermal expansion and dehydration of brushite, di-calcium phosphate dihydrate

Received: 15 May 2004 / Accepted: 27 July 2004

Abstract The unit-cell and atomic parameters of per-deuterated brushite have been extracted from Rietveld analysis of neutron powder diffraction data within the temperature range 4.2 to 470 K. The thermal expansion of brushite is anisotropic, with the largest expansion along the *b* axis due principally to the effect of the O(1)···D(4) and O(3)···D(2) hydrogen bonds. Expansion along the *c* axis, influenced by the Ow1···D(5) interwater hydrogen bond, is also large. The high temperature limits for the expansion coefficients for the unit-cell edges *a*, *b* and *c* are $9.7(5) \times 10^{-6}$, $3.82(9) \times 10^{-5}$ and $5.54(5) \times 10^{-5}$ K^{-1}, respectively, and for the cell volume it is $9.7(1) \times 10^{-5}$ K^{-1}. The β angle displays oscillatory variation, and empirical data analysis results in $\alpha_\beta = 1.28(3) \times 10^{-6}\sin(0.0105\ T)$ K^{-1}, within this temperature range. The evolution of the thermal expansion tensor of brushite has been calculated between $50 \leq T \leq 400$ K. At 300 K the magnitudes of the principal axes are $\alpha_{11} = 50(6) \times 10^{-6\ K-1}$, $\alpha_{22} = 26.7(7) \times 10^{-6}$ K^{-1} and $\alpha_{33} = 7.0(5) \times 10^{-6}$ K^{-1}. The intermediate axis, α_{22}, is parallel to **b**, and using IRE convention for the tensor orthonormal basis, the axes α_{11} and α_{33} have directions equal to (−0.228, 0, −0.974) and (−0.974, 0, 0.228) respectively. Under the conditions of these experiments, the onset of dehydration occurred at temperatures above 400 K. Bond valence analysis combined with assessments of the thermal evolution of the bonding within brushite suggests that dehydration is precipitated through instabilities in the chemical environment of the second water molecule.

P. F. Schofield (✉) · K. S. Knight · J. A. M. van der Houwen
E. Valsami-Jones
Department of Mineralogy, Natural History Museum,
Cromwell Road, London. SW7 5BD. UK
e-mail: pfs@nhm.ac.uk
Tel: +44 (0)207-942-5184
Fax: +44 (0)207-942-5537

K. S. Knight
ISIS Science Division, Rutherford Appleton Laboratory,
Chilton, Didcot, OX11 0QX. UK

Keywords Brushite · Thermal expansion · Dehydration · Neutron powder diffraction · Di-calcium phosphate didydrate

Introduction

Brushite, $CaHPO_4 2H_2O$, is a less common calcium phosphate than apatite, found in caves (Fiore and Laviano 1991; Onac et al. 2001) and phosphate deposits (Nriagu 1984), but also known to form soon after soluble fertilizers have been applied to soils, where it can persist for many years in a range of conditions (Fixen et al. 1983). In recent years, research on calcium phosphates has attracted considerable interest, due to a number of emerging significant applications. These include their potential as protonic conductors within brushite-based composites (Tortet et al. 1997, 1998), but also remediation media, wastewater treatment by-products, ceramics, nutrient supplements and stabilizers for plastics. The uncontrolled precipitation of calcium phosphates in wastewater systems, pathological minerals and their potential in repairing bone/tooth damage are important problems for the future. Effective control of calcium phosphate formation, however, remains a challenge.

Apatite is the most common and stable member of the calcium phosphate minerals. Several studies have proposed that brushite, along with other calcium phosphates such as octacalcium phosphate, tricalcium phosphate, monetite and whitlockite, play a crucial, albeit transient, role in many biological and engineered systems, acting as intermediary phases in the crystallization of the more stable hydroxyl-apatite (Francis and Webb 1971; Roufosse et al. 1979; Abbona and Franchini-Angela 1990). Brushite is believed to represent the precursor phase of apatite in environments of $pH < 7$ and at $pH < 5$ brushite is the most stable calcium phosphate (Koutsoukos 1998).

Wastewater treatment currently involves the removal of phosphorus by chemical or biological means,

followed by disposal of the final phosphorus-containing sludge; phosphate can represent 30–40% of the sludge. While there is a growing need to recycle this phosphorus, the retrieval of phosphate prior to disposal of the sludge has been problematic. This is due to sluggish phosphate nucleation, low phosphorus levels in the product and high production costs amongst other reasons (e.g. Valsami-Jones 2001). A complete understanding of the crystallization and kinetics of hydroxyapatite formation, particularly the mechanism pathways through its precursor phases, will enable an improvement in current technology that will hopefully result in economically viable processes for phosphorus recovery.

Crystal structure

The crystal structure of brushite was first solved by Beevers (1958) using X-ray single-crystal diffraction, and Jones and Smith (1962), again using X-ray methods, attempted to locate the hydrogen atoms. Accurate atomic coordinates of the hydrogen atoms were finally obtained by Curry and Jones (1971) using neutron single-crystal diffraction, and this structure has been accurately reproduced through first-principles calculations by Sainz-Díaz et al. (2004). Although the structure is topologically analogous to that of the sulphate analogue gypsum, $CaSO_4 2H_2O$ (Pederson and Semmingson 1982), brushite displays a distinct piezoelectric effect and, like the arsenic analogue pharmacolite, $CaHAsO_4 2H_2O$ (Ferraris 1969; Ferraris et al. 1971), crystallizes in the non-centrosymmetric space group *Ia*.

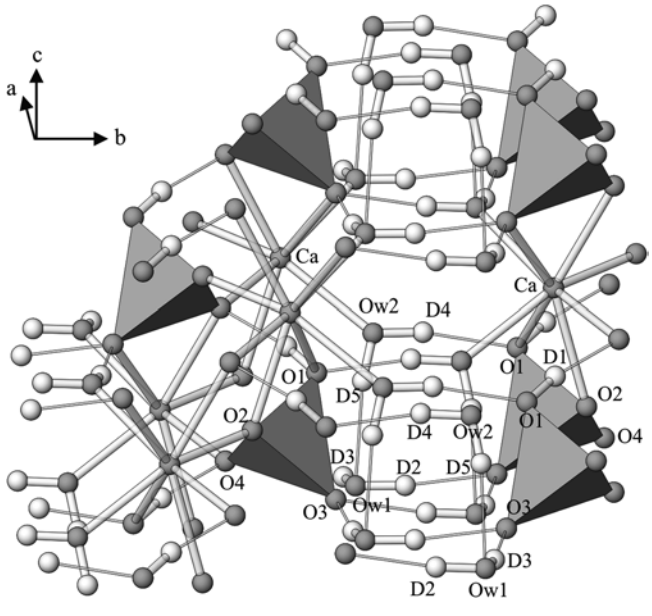

Fig. 1 Representation of the crystal structure of brushite viewed along the *a* axis with the *b* axis horizontal and the *c* axis vertical. The H (D) atoms are shaded *light grey*, the Ca and O atoms are shaded *dark grey*, and the PO_4 units are shown as *solid tetrahedra*

The crystal structure (Fig. 1) is basically a layer structure bound together by hydrogen bonding. Zig-zag chains of CaO_8 polyhedra running parallel to the *a* axis are bound together by similar zig-zag chains of PO_4^{3-} tetrahedra, resulting in corrugated sheets normal to the *b* axis. These sheets are weakly bound together through hydrogen bonding associated with a layer of H_2O molecules. The phosphate tetrahedra are asymmetric, containing four non-equivalent P–O bond lengths; the longest of these P–O bonds involves a hydroxyl oxygen where the acidic proton resides. This acidic proton forms a short hydrogen bond of 1.69 Å to O(4) in which the O–H···O angle is 167.9° (Curry and Jones 1971). Two of the oxygen atoms bonded to the Ca^{2+} cations belong to H_2O molecules and the remaining six oxygen atoms are bonded to the phosphate groups.

The H_2O molecules form a layer which binds together the polyhedral layers via the O(1)···H(4) and O(3)···H(2) hydrogen bonds, which act almost entirely along the *b* axis. Single-crystal ^1H NMR (Jones and Smith 1960) and infrared studies (Berry and Baddiel 1967; Petrov et al. 1967) suggested that the two water molecules are distorted from that of free water molecules and non-equivalent, and this was subsequently confirmed by the neutron single-crystal study of Curry and Jones (1971). The H–O–H bond angles of these H_2O molecules are 106.6° and 105.4° and the mean H–O bonds in each water molecule are 0.97 and 0.945 Å, respectively. One of the water molecules has near linear O–H···O hydrogen bonds with angles of 175.7° and 173.3°, while the second water molecule has hydrogen bonds with angles of 167.3° and 165.8° (Curry and Jones 1971). One further difference between the crystal structures of brushite and gypsum is the reported interwater hydrogen bond present in brushite (Curry and Jones 1971) but absent in gypsum, where the hydrogen bonding occurs only between the water and sulphate molecules.

As the crystal structures of brushite and gypsum are analogous and topologically identical, it may be expected that the temperature-dependent behaviour of brushite, prior to the onset of dehydration, would mimic that of gypsum. The thermal expansion of gypsum is highly anisotropic along the *b* axis due principally to the effect of the H2···O1 hydrogen bond, and the β angle displays an oscillatory temperature variation. (Schofield et al. 1996; Knight et al. 1999). While gypsum dehydrates to the metastable hemihydrate, basanite, brushite dehydrates initially to monetite, $CaHPO_4$, at 150–180 °C and then further deprotonates to form γ-calcium pyrophosphate (γ-$Ca_2P_2O_7$) at 320 °C. γ-$Ca_2P_2O_7$ subsequently transforms to the β- and α-calcium pyrophosphates at temperatures of 700 and 1200 °C, respectively (McIntosh and Jablonski 1956; Wikholm et al. 1975). We have used time-of-flight neutron powder diffraction methods to study the thermal behaviour of the brushite lattice and the atomic mechanisms controlling this behaviour up to the point of dehydration.

Experimental

Synthesis

Due to the large incoherent cross-section for the scattering of thermal neutrons from protons, it was necessary to prepare a deuterated sample for powder diffraction experiments in order to avoid large backgrounds and improve signal to noise. The material used for these experiments was synthesized by direct precipitation. Synthesis was performed just prior to the commencement of the experiment to minimize the possibility of H↔D exchange occurring.

Deuterated brushite was synthesized by direct precipitation from solution at room temperature using a method similar to that in Elliott (1994) whereby a solution of $CaCl_2$ was slowly added to a solution of $Na_2HPO_4.2H_2O$ and KH_2PO_4. To ensure a deuterated product, all solutions were prepared using D_2O. Throughout the synthesis the solution pH was maintained between 4 and 5 by manual addition of a solution of KH_2PO_4 in D_2O. The white precipitate comprised needle-like crystals with a maximum length of about 500 μm and other dimensions below 50 μm.

The synthetic product was charactezised using X-ray powder diffraction to confirm that it was single-phase brushite, and infrared spectroscopy to confirm that the brushite was deuterated (Farmer 1974). In addition to the large incoherent scattering cross-section of protium, there is a difference in both magnitude and sign for the coherent scattering lengths of protium (−3.739 fm) and deuterium (6.671 fm) (Sears 1992). The large incoherent scattering of neutrons caused by hydrogen can be used to qualitatively assess the degree of deuteration of the sample. The low background intensity indicates that the deuteration of the brushite was very high, while attempts to refine the data incorporating protons in the model indicated that the D content was above 99% of the expected total.

Neutron diffraction

Neutron time-of-flight powder diffraction data were collected on the medium resolution diffractometer POLARIS (Smith et al. 1994) at the ISIS neutron spallation source, Rutherford Appleton Laboratory, UK (Wilson 1995). Just under 2 g of perdeuterated brushite were packed into an indium-sealed cylindrical vanadium can with an external diameter of 11 mm. The sample was quenched in liquid nitrogen before being placed in a cryofurnace and cooled to 4.2 K. Diffraction patterns were collected for a total of 350 μA h between 4.2 and 275 K and for a total of 300 μA h between 300 and 470 K. Neutron diffraction data were collected initially at 4.2 K, then 10 K and at intervals of 10 to 100 K, above which the temperature interval was 25 to 400 K. After the sample temperature had increased to the set point, and prior to the collection of the diffraction data, there was an equilibration time of 10 min.

Data were collected simultaneously in three separate detector banks set at mean scattering angles of $2\theta = 35°$, 90° and 145° in the time-of-flight ranges 2000 to 17600 μs, 2000 to 19100 μs and 2000 to 19500 μs, respectively. Data were binned as $\Delta t/t = 0.0005$, 0.0005 and 0.002 for the detector banks at $2\theta = 35°$, 90° and 145°, respectively, cryofurnace background subtracted, normalized to the incident flux distribution using the isotropic incoherent scattering from a vanadium rod and were finally corrected for absorption and self-scattering. These data were subsequently used in a three-bank Rietveld profile refinement.

Data refinement

Unit-cell parameters and atomic coordinates were extracted from Rietveld profile refinements of the neutron powder diffraction data and were carried out using GSAS (Larson and Von Dreele 1994). The first refinement was performed on the data collected at 4.2 K using the coherent scattering lengths from Sears (1992) (Ca 4.70 fm, P 5.13 fm, O 5.803 fm and D 6.671 fm) with the starting model based on the coordinates of Curry and Jones (1971). The converged

Table 1 Experimental and refinement details

T (K)	Count time (μA h)	Total no. of observations	Total no. of variables	R_p (%)	R_{wp} (%)	R_{exp} (%)	Reduced χ^2
4.2	350	10143	92	3.72	2.29	1.73	1.75
10	350	10144	92	3.67	2.14	1.58	1.82
20	350	10144	92	3.43	2.02	1.51	1.80
30	350	10144	92	3.66	2.21	1.67	1.76
40	350	10144	92	3.66	2.22	1.67	1.78
50	350	10144	92	3.66	2.13	1.59	1.81
60	350	10144	92	3.43	2.08	1.55	1.80
70	350	10144	92	3.18	1.84	1.37	1.82
80	350	10144	92	3.31	1.94	1.44	1.83
90	350	10144	92	3.35	1.96	1.44	1.84
100	350	10144	92	3.53	2.08	1.57	1.75
125	350	10144	92	3.44	2.07	1.53	1.83
150	350	10144	92	3.28	1.94	1.43	1.84
175	350	10144	92	3.17	1.92	1.40	1.88
200	350	10144	92	3.13	1.91	1.40	1.87
225	350	10144	92	3.24	1.97	1.42	1.93
250	350	10144	92	3.28	2.01	1.45	1.92
275	350	10144	92	3.50	2.09	1.48	1.99
300	300	10144	92	3.62	2.14	1.59	1.81
325	300	10144	92	3.94	2.36	1.78	1.75
350	300	10144	92	3.62	2.21	1.60	1.90
375	300	10144	92	3.57	2.13	1.63	1.71
400	300	10144	92	3.97	2.23	1.87	1.42
425	300	10144	92	3.49	1.93	1.55	1.56
450	300	10144	92	3.73	2.14	1.68	1.62
460	300	10144	92	3.82	2.21	1.69	1.71
470	300	7907	44	3.84	2.33	1.95	1.43

parameters for this refinement were then used as the initial dataset for the subsequent refinement, in this case for the patterns at 10 K, and so on for the remaining temperatures up to 400 K. Data from three detector banks were refined simultaneously with 92 variables and 10144 observations per refinement. For each refinement and histogram, the histogram scale factor and background (consisting of ten Chebyshev polynomial terms) were initially refined before the unit-cell parameters, atom coordinates and the isotropic atomic displacement parameters were included in the overall refinement. The goodness-of-fit parameters, refinement and experimental details are summarized in Table 1.

Above 400 K there was a trace of a second phase in the diffraction patterns, suggesting that dehydration may have begun; the fraction of this possible dehydration product remained very low up to 460 K. At 470 K brushite was no longer the major phase. As the single-phase nature of the sample was uncertain and there was the possibility, albeit slight, that the sample was dehydrating during data collection at temperatures above 400 K, subsequent modelling was limited to the temperature range 4.2 to 400 K.

The structure refined at 300 K compares well with that of the neutron single-crystal study of Curry and Jones (1971) and the calculations of Sainz-Díaz et al. (2004), and a bond valence analysis using the 300 K data from this study shows that the bonding within the structure is fairly well balanced and confirms the existence of the interwater molecule hydrogen bond. From the bond valence analysis it can be seen that D3 is somewhat overbonded with respect to the other D atoms, and that O1, O4 and Ow1 may also be slightly overbonded.

Lattice expansion

The lattice parameters, extracted from the Rietveld analyses, for perdeuterated brushite within the temperature range 4.2 to 400 K are given in Table 2 and displayed in Fig. 2. These data show that the thermal expansion of brushite is anisotropic, with the *b* and *c* lattice parameters increasing by 0.093 and 0.083 Å, respectively, while the *a* lattice parameter increases by only 0.016 Å. The β angle shows a small total variation across the entire temperature range; however, this variation is oscillatory as a function of temperature, with the maximum change amounting to about 0.024°. The increase in the volume is 10.93 Å^3, which represents some 2.25% of the volume at 4.2 K, and principally reflects the anisotropy along the *b* axis.

On increasing temperature the three cell edges vary in the expected manner, with little initial response followed by a near-linear increase as a function of increasing temperature. The onset of significant expansion does not occur at the same temperature for these cell edges, with *a*, *b* and *c* showing minimal or no increases below about 50, 100 and 40 K, respectively.

Somewhat unusually, the β angle appears to have an oscillatory variation across the temperature range investigated; that is, the sign of the thermal expansion profile changes at a certain temperature. The β angle appears to be unchanged up to about 50 K, although the slight data scatter over the first 50 K makes this difficult to confirm. Above about 50 K the β angle decreases almost linearly as a function of temperature until 300 K, above which it shows a rapid increase up to 400 K. Such anomalous behaviour in the β angle is not evident in the volume expansion, which appears to vary in the expected manner, and is dominated by the large expansion along the *b* axis.

The trends for the unit-cell edges are well fitted to an Einstein expression of the form $X = X_0 + K/(e^{(\vartheta/T)} - 1)$, where X_0 is the parameter X at zero Kelvin, K is the Einstein constant, T is the temperature in Kelvin

Table 2 Lattice parameters of deuterated brushite from 4.2K to 470 K

Temp (K)	*a* (Å)	*b* (Å)	*c* (Å)	β	Volume (Å^3)
4.2	5.79903(6)	15.1254(2)	6.18398(7)	116.429(1)	485.724(7)
10	5.7990(1)	15.1255(3)	6.1839(1)	116.428(1)	485.73(2)
20	5.7991(1)	15.1251(3)	6.1840(1)	116.429(1)	485.73(2)
30	5.7990(1)	15.1255(3)	6.1839(1)	116.427(1)	485.73(2)
40	5.7991(1)	15.1253(3)	6.1842(1)	116.428(1)	485.75(2)
50	5.7992(1)	15.1256(3)	6.1844(1)	116.426(1)	485.80(2)
60	5.7994(1)	15.1250(3)	6.1850(1)	116.426(1)	485.83(2)
70	5.7997(1)	15.1257(3)	6.1857(1)	116.425(1)	485.94(2)
80	5.8000(1)	15.1256(3)	6.1866(1)	116.422(1)	486.05(2)
90	5.8003(1)	15.1259(3)	6.1873(1)	116.422(1)	486.14(2)
100	5.8007(1)	15.1267(3)	6.1887(1)	116.419(1)	486.32(2)
125	5.8016(1)	15.1284(3)	6.1916(1)	116.418(1)	486.68(2)
150	5.8026(1)	15.1314(3)	6.1956(1)	116.416(1)	487.19(2)
175	5.8040(1)	15.1361(3)	6.2006(1)	116.414(1)	487.85(2)
200	5.8053(1)	15.1420(3)	6.2060(1)	116.413(1)	488.59(2)
225	5.8062(1)	15.1482(3)	6.2118(1)	116.410(1)	489.32(2)
250	5.8077(1)	15.1563(3)	6.2186(1)	116.408(1)	490.26(2)
275	5.8091(1)	15.1656(3)	6.2259(2)	116.407(1)	491.26(3)
300	5.8105(1)	15.1758(4)	6.2337(2)	116.405(1)	492.34(3)
325	5.8119(1)	15.1867(4)	6.2416(2)	116.405(1)	493.43(3)
350	5.8132(2)	15.1973(4)	6.2497(2)	116.406(1)	494.53(3)
375	5.8145(2)	15.2086(4)	6.2580(2)	116.408(1)	495.66(3)
400	5.8151(2)	15.2179(4)	6.2664(2)	116.413(1)	496.65(3)
425	5.8140(2)	15.2235(5)	6.2744(2)	116.425(1)	497.32(4)
450	5.8152(3)	15.2361(7)	6.2851(3)	116.439(2)	498.62(5)
460	5.8147(3)	15.2420(8)	6.2894(4)	116.447(2)	499.08(6)
470	5.8135(3)	15.2422(9)	6.2919(3)	116.456(4)	499.15(3)

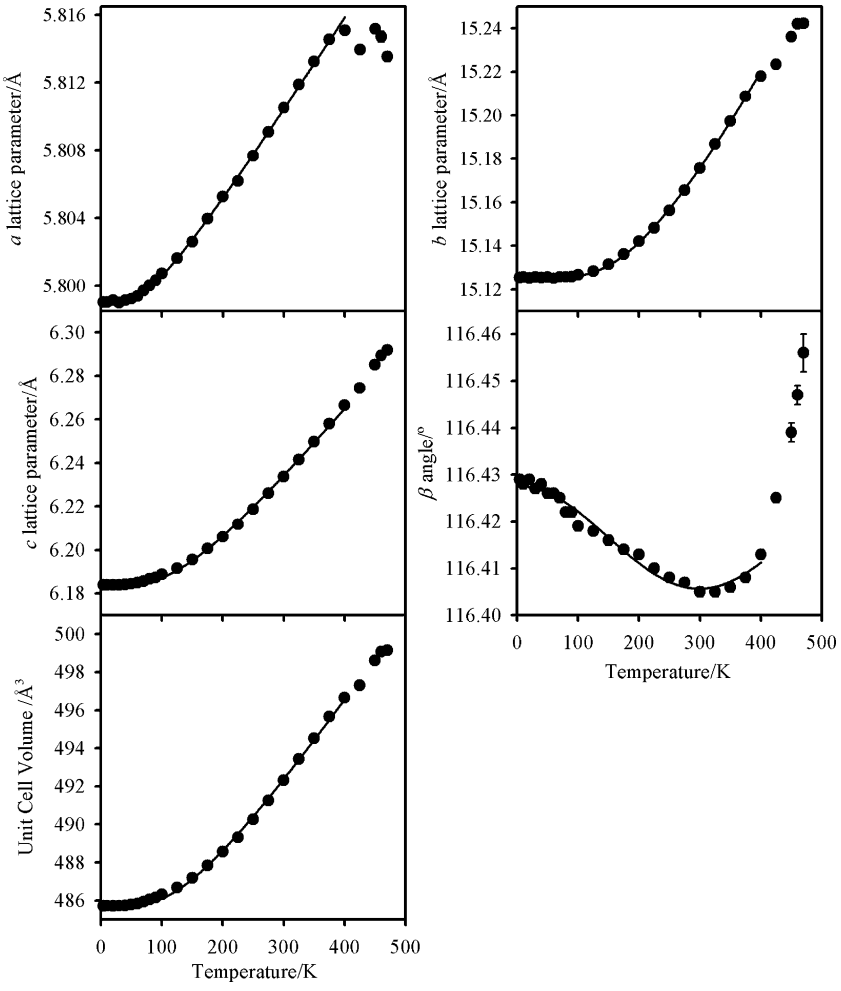

Fig. 2 Variation of the lattice parameters of brushite within the temperature range $4.2 \leq T \leq 470$ K. The refined parameters are shown for the full temperature range while the calculated fits are for the temperature range $4.2 \leq T \leq 400$ K. The models are represented by Einstein functions for all parameters except the β angle, that was empirically fitted by a cosine function

between 4.2 and 400 K, and ϑ is the effective Einstein temperature. As the β-cell angle showed oscillatory behaviour, it was fitted empirically with a cosine function of the form $\beta = \beta' + A\cos(\omega T)$, oscillating around β' with an amplitude A and effective angular frequency ω. Fitting the temperature dependence of the β angle to a cosine function does, however, result in finite changes at temperatures below 50 K. These fits are displayed with the raw data graphically in Fig. 2, and are tabulated with the associated errors derived from the fitting process in Table 3.

The instantaneous (isobaric) thermal expansion is related to the unit cell parameter x, where $\alpha_x = (1/x_0)(\delta x/\delta T)$ and x_0 is the magnitude of parameter x at zero Kelvin. At high temperatures $e^{(\vartheta/T)} \approx 1 + (\vartheta/T)$, using a Taylor's expansion, and consequently $(1/x_0)(\delta x/\delta T) \approx K/(x_0\vartheta).[1 + (\vartheta/T)]$, giving, for the cell edges

$$\alpha_a = (1/a_0\delta a/\delta T) \approx K/(a_0\vartheta).[1 + (\vartheta/T)] = 9.71(5) \times 10^{-6}[1 + (\vartheta/T)] \quad (1)$$

$$\alpha_b = (1/b_0)(\delta b/\delta T) \approx K/(b_0\vartheta).[1 + (\vartheta/T)] = 3.82\,(9) \times 10^{-5}[1 + (\vartheta/T)] \quad (2)$$

$$\alpha_c = (1/c_0)(\delta c/\delta T) \approx K/(c_0\vartheta).[1 + (\vartheta/T)] = 5.54\,(5) \times 10^{-5}[1 + (\vartheta/T)] \quad (3)$$

$$\alpha_{vol} = (1/V_0)(\delta V/\delta T) \approx K/(V_0\vartheta).[1 + (\vartheta/T)] = 9.7\,(1) \times 10^{-5}[1 + (\vartheta/T)], \quad (4)$$

Table 3 Tabulated results and errors from the lattice parameter fitting procedures for the data in the range $4.2\ \text{K} \leq T \leq 400$ K

	X_0	K	ϑ
a	5.7991(1) Å	0.0125(5)	222(7) K
b	15.1255(1) Å	0.367(8)	634(6) K
c	6.1846(1) Å	0.135(1)	394(2) K
v	485.78(1) Å^3	19.2(2)	409(2) K

	β'	A	ω	β_0
β	116.4166(2)	0.0110(3)	0.0105(1)	116.4276(4)

Note: X_0, K and ϑ represent the zero Kelvin cell parameter value, the Einstein constant and the effective Einstein temperatures, respectively. The data from the empirical cosine fit to the β angle variation reflects oscillation about β', amplitude A, effective angular frequency ω

and the instantaneous thermal expansion for the β-cell angle, reflecting the change in sign of the thermal expansion, is

$$\alpha_\beta = (1/\beta_0)(\delta\beta/\delta T) = -(A\omega/\beta_0)\sin(\omega T)$$
$$= 1.28(3) \times 10^{-6}\sin(0.0105T). \quad (5)$$

The influence of the temperature upon the thermal expansion can be seen from Eq (1) to (5). For a, b, c and the cell volume the rate of decrease of the thermal expansion coefficient decreases as the temperature increases, leading to high temperature limits of $9.7(5) \times 10^{-6}$, $3.82(9) \times 10^{-5}$, $5.54(5) \times 10^{-5}$ and $9.7(1) \times 10^{-5}$ K^{-1}, respectively.

Thermal expansion tensor

In the case of single crystals, Jessen and Kuppers (1991) found that increased precision in the calculation of the thermal expansion tensor of monoclinic and triclinic crystals could be achieved by direct least-squares determination of the tensor coefficients, α_{ij}, from the changes in the lattice spacings of a limited number of reflections. They found that the normally accepted method, which requires firstly the calculation of the temperature dependence of the lattice parameters, and then a subsequent analysis of the tensor coefficients, gave rise to significant error propagation. However, in the case of powder data, Knight (1996) argued that model-

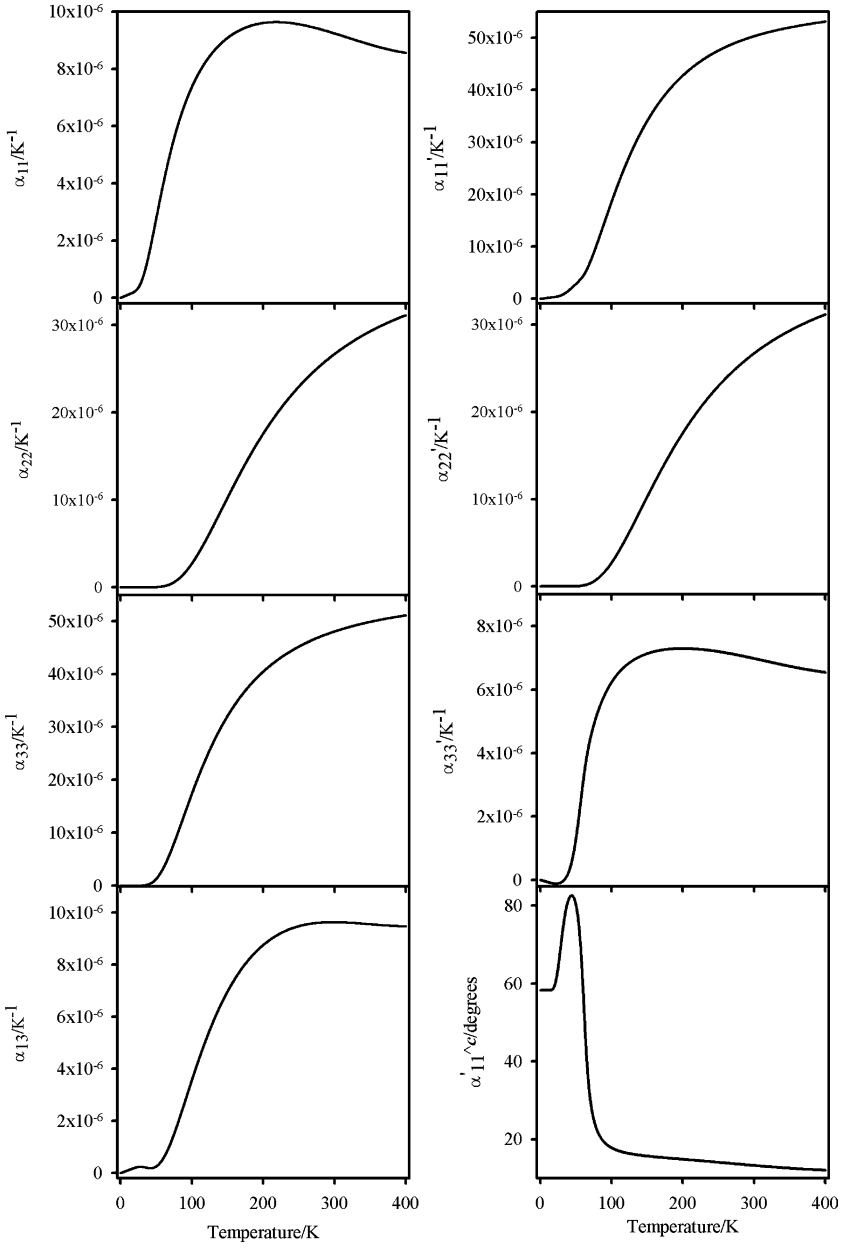

Fig. 3 Temperature dependence of the thermal expansion tensor coefficients, α_{11}, α_{22}, α_{33} and α_{13} (*left*) and the magnitudes of the principal thermal expansion tensors and the angle of orientation of the principal axis α_{11} (*right*) as calculated from the unit-cell parameters

independent profile fitting of entire powder diffraction datasets, in which all reflections contribute to the lattice parameter determinations, is sufficiently accurate and precise to be a method superior to that proposed by Jessen and Kuppers (1991). Indeed, this has been used for neutron powder diffraction data of the structurally analogous mineral gypsum (Knight et al. 1999).

Using the IRE (Institute of Radio Engineers) convention for the orthonormal tensor basis: $\mathbf{e}_3 \parallel \mathbf{c}$, $\mathbf{e}_2 \parallel \mathbf{b}^*$, $\mathbf{e}_1 \parallel \mathbf{e}_2 \times \mathbf{e}_3$, the Lagrangian thermal expansion tensor coefficients for a monoclinic crystal with b as the unique axis are:

$$\alpha_{11}(T) = \frac{1}{a_0 \sin\beta_0}\left[\sin\beta\frac{da}{dT} + a\cos\beta\frac{d\beta}{dT}\right] \quad (6)$$

$$\alpha_{22}(T) = \frac{1}{b_0}\frac{db}{dT} \quad (7)$$

$$\alpha_{33}(T) = \frac{1}{c_0}\frac{dc}{dT} \quad (8)$$

$$\alpha_{13}(T) = \frac{1}{a_0}\frac{da}{dT}\left[\frac{1}{\sin 2\beta_0} - \frac{\sin\beta}{2\cos\beta_0}\right] - \frac{a\cos\beta}{2a_0\cos\beta_0}\frac{d\beta}{dT} - \frac{\cot\beta_0}{2c_0}\frac{dc}{dT} \quad (9)$$

(Schlenker et al. 1975) and the temperature evolution of these coefficients is shown in Fig. 3. Using the parameters derived from the least-squares fitting of the temperature dependence of the lattice parameters, we determined the temperature variation of the thermal expansion tensor coefficients for brushite between 4.2 and 400 K. The principal axes and their orientation were determined by standard methods of eigenvalue and eigenvector decomposition. Assessment of the temperature dependence of both the eigenvalues and eigenvectors within the **a**–**c** plane showed non-physical behaviour at temperatures below about 50 K (one oscillatory eigenvalue and rapid change in the orientation of the associated eigenvector) and probably arises from the empirical parameterization of β(T) as a cosine curve. Consequently, subsequent discussion will consider only the temperature range $50 \le T \le 400$ K. The temperature dependence of the principal axes' magnitudes and the angle of orientation of the principal axis α_{11} with respect to c are shown in Fig. 3.

The magnitudes of the maximum and intermediate principal axes (α_{11} and α_{22} respectively) show regular behaviour, with α_{11} appearing to saturate close to 5.3×10^{-5} K^{-1}. α_{22} reaches a value of 3.11×10^{-5} K^{-1} at 400 K, although this axis does not appear to have reached saturation, perhaps due to the approaching onset of dehydration. Rather than saturating, the magnitude of the minimum principal axis (α_{33}) reaches a maximum of about 7.3×10^{-6} K^{-1} at about 200 K, before decreasing gradually and becoming about 6.5×10^{-6} K^{-1} at 400 K. The angle of orientation of the principal axis α_{11} with respect to **c** decreases as a function of increasing temperature, with α_{11} rotating away from **c** towards **a** from ~18° at 100 K to ~12° at 400 K. At 300 K the principal axes have magnitudes and directions; α_{11}, $50(6) \times 10^{-6}$ K^{-1} (−0.228, 0, −0.974), α_{22}, $26.7(7) \times 10^{-6}$ K^{-1} (0, 1, 0), α_{33}, $7.0(5) \times 10^{-6}$ K^{-1} (−0.974, 0, 0.228).

Thermal expansion of the brushite structure

The structural parameters at temperatures up to 400 K for brushite that have been extracted from the Rietveld refinements are provided in Table 4 and the variation of selected bond lengths are shown in Figs. 4,6 and 8–10. The Ca atoms are bonded to eight O atoms, of which six belong to PO_4 groups and two belong to water molecules. The Ca–O bonds involving phosphate groups all increase as the temperature is increased, with the Ca–O3 bond increasing almost linearly by 1.5% (0.039 Å) and an apparent anomalous decrease occurring between 60 and 90 K. Ca–O1, Ca–O2 and Ca–O4 all vary in a more expected style, with no or minimal change at the lowest temperatures and an overall total increase of 0.0266, 0.0299 and 0.013 Å, amounting to some 1, 1.2 and 0.5%, respectively. The Ca–O2′ and Ca–O4′ bonds show slightly unusual behaviour, with Ca–O2′ reaching a maximum at around 300–325 K before apparently decreasing rapidly up to 400 K and the Ca–O4′ bond showing no increase below 300 K. The overall increase for these two bonds is 0.0133 Å (0.6%) for Ca–O2′ and 0.0277 Å (1.2%) for Ca–O4′. Both of the Ca–O bonds that involve the O atoms of the water molecules show slightly unusual behaviour as a function of increasing temperature, with the Ca–Ow1 bond showing no change up to about 300 K, and Ca–Ow2 showing oscillatory variation by decreasing above about 50–60 K, reaching a minimum at about 300 K and increasing thereafter. The combined effect of these bond-length changes is such that there is only a gradual increase in the volume of the CaO_8 polyhedra up to about 275 K, above which the rate of increase is significantly greater (Fig. 5).

Within the phosphate tetrahedra of the HPO_4^{2-} groups, P-O1 and P-O2 both decrease in length, over the whole temperature range, by about 1.3% (0.0212 Å) and 0.8% (0.0118 Å), respectively but, while the decrease in the P-O1 bond length begins at about 100 K, the P-O2 bond length decreases only slightly until about 300 K, at which point the decrease becomes more dramatic. P-O4 increases by about 1.3% (0.0203 Å) over the entire temperature range although little change is evident between 4.2 and about 275 K. The P-O3 bond, however, shows initially increases above about 100 K but at about 300 K decreases rapidly such that the overall increase between 4.2 and 400 K is only 0.2% (0.0029 Å). The bond angles of the phosphate tetrahedra are also shown in Fig. 6, where again it can be seen that the largest variation occurs at about 275–300 K, and the O2-P-O4 and O2-P-O3 angles show oscillatory behaviour as a function of temperature. Indeed, there is no change in the angular variance of the phosphate tetrahedral until about 300 K, at which point there is a sharp decrease.

Table 4a Atomic coordinates of deuterated brushite from 4.2 to 125 K (Uiso values are ×100)

	4.2 K	10 K	20 K	30 K	40 K	50 K	60 K	70 K	80 K	90 K	100 K	125 K
Ca *x*	0.5	0.5	0.5	0.5	0.5	0.5	0.5	0.5	0.5	0.5	0.5	0.5
Ca *y*	0.3274(1)	0.3274(1)	0.3275(1)	0.3273(1)	0.3273(1)	0.3273(1)	0.3275(1)	0.3273(1)	0.3274(1)	0.3274(1)	0.3276(1)	0.3272(2)
Ca *z*	0.25	0.25	0.25	0.25	0.25	0.25	0.25	0.25	0.25	0.25	0.25	0.25
Ca Uiso	0.38(3)	0.36(3)	0.41(3)	0.34(3)	0.39(3)	0.40(3)	0.47(4)	0.43(3)	0.44(4)	0.47(4)	0.49(4)	0.51(4)
P *x*	−0.0094(6)	−0.0100(6)	−0.0091(6)	−0.0092(6)	−0.0095(6)	−0.0095(6)	−0.0085(6)	−0.0088(6)	−0.0089(6)	−0.0101(6)	−0.0098(6)	−0.0097(6)
P *y*	0.3227(1)	0.3227(1)	0.3226(1)	0.3228(1)	0.3226(1)	0.3228(1)	0.3227(1)	0.3227(1)	0.3227(1)	0.3227(1)	0.3225(1)	0.3225(1)
P *z*	0.7285(5)	0.7280(5)	0.7282(5)	0.7281(5)	0.7288(5)	0.7280(5)	0.7288(5)	0.7283(5)	0.7285(5)	0.7272(5)	0.7284(5)	0.7280(6)
P Uiso	0.02(2)	0.04(2)	0.04(2)	0.02(2)	0.05(2)	0.05(2)	0.03(2)	0.07(3)	0.05(3)	0.04(3)	0.06(3)	0.08(3)
O1 *x*	−0.0097(5)	−0.0098(5)	−0.0094(5)	−0.0096(5)	−0.0097(5)	−0.0093(6)	−0.0088(6)	−0.0096(6)	−0.0098(6)	−0.0103(6)	−0.0098(6)	−0.0102(6)
O1 *y*	0.3679(1)	0.3680(1)	0.3680(1)	0.3678(1)	0.3680(1)	0.3680(1)	0.3681(1)	0.3680(1)	0.3678(1)	0.3679(1)	0.3679(1)	0.3678(1)
O1 *z*	−0.0351(5)	−0.0356(5)	−0.0353(5)	−0.0355(5)	−0.0352(5)	−0.0356(5)	−0.0348(5)	−0.0357(5)	−0.0355(5)	−0.0364(5)	−0.0357(5)	−0.0366(5)
O1 Uiso	0.40(3)	0.37(3)	0.36(3)	0.46(3)	0.38(3)	0.38(3)	0.38(3)	0.42(3)	0.45(3)	0.51(3)	0.52(3)	0.53(3)
O2 *x*	0.2556(5)	0.2553(5)	0.2560(5)	0.2561(5)	0.2556(5)	0.2556(5)	0.2559(5)	0.2558(5)	0.2556(5)	0.2556(5)	0.2554(5)	0.2554(5)
O2 *y*	0.2819(1)	0.2819(1)	0.2819(1)	0.2819(1)	0.2817(1)	0.2819(1)	0.2817(1)	0.2817(1)	0.2819(1)	0.2819(1)	0.2819(1)	0.2819(1)
O2 *z*	0.8215(5)	0.8209(5)	0.8213(5)	0.8210(5)	0.8216(5)	0.8213(5)	0.8222(5)	0.8212(5)	0.8214(5)	0.8210(5)	0.8214(5)	0.8217(5)
O2 Uiso	0.25(2)	0.26(3)	0.24(2)	0.30(3)	0.27(3)	0.27(3)	0.29(3)	0.29(3)	0.33(3)	0.33(3)	0.35(3)	0.38(3)
O3 *x*	−0.0650(5)	−0.0647(5)	−0.0639(5)	−0.0644(5)	−0.0640(5)	−0.0642(5)	−0.0633(5)	−0.0636(5)	−0.0637(6)	−0.0643(6)	−0.0636(6)	−0.06324(6)
O3 *y*	0.3933(1)	0.3933(1)	0.3933(1)	0.3933(1)	0.3933(1)	0.3934(1)	0.3933(1)	0.3933(1)	0.3934(1)	0.3934(1)	0.3933(1)	0.3933(1)
O3 *z*	0.5415(5)	0.5408(5)	0.5415(5)	0.5411(5)	0.5419(5)	0.5413(5)	0.5420(5)	0.5411(5)	0.5412(5)	0.5407(6)	0.5413(5)	0.5409(6)
O3 Uiso	0.34(3)	0.37(3)	0.36(3)	0.37(3)	0.35(3)	0.36(3)	0.40(3)	0.41(3)	0.45(3)	0.46(3)	0.45(3)	0.60(3)
O4 *x*	0.7791(5)	0.7794(6)	0.7797(6)	0.7794(5)	0.7796(6)	0.7791(6)	0.7802(6)	0.7797(6)	0.7799(6)	0.7787(6)	0.7789(6)	0.7795(6)
O4 *y*	0.2532(1)	0.2531(1)	0.2531(1)	0.2537(1)	0.2532(1)	0.2532(1)	0.2530(1)	0.2530(1)	0.2531(1)	0.2530(1)	0.2531(1)	0.2529(1)
O4 *z*	0.6355(5)	0.6349(5)	0.6352(5)	0.6352(5)	0.6357(5)	0.6352(5)	0.6359(5)	0.6350(5)	0.6358(5)	0.6348(5)	0.6347(5)	0.6342(6)
O4 Uiso	0.12(2)	0.14(2)	0.15(2)	0.14(2)	0.17(2)	0.15(2)	0.16(2)	0.18(2)	0.18(3)	0.21(3)	0.23(3)	0.26(3)
Ow1 *x*	0.3676(6)	0.3672(6)	0.3680(6)	0.3677(5)	0.3673(6)	0.3675(6)	0.3678(6)	0.3671(6)	0.3674(6)	0.3666(6)	0.3668(6)	0.3665(6)
Ow1 *y*	0.4258(1)	0.4258(1)	0.4258(1)	0.4258(1)	0.4258(1)	0.4258(1)	0.4256(1)	0.4258(1)	0.4258(1)	0.4256(1)	0.4256(1)	0.4256(1)
Ow1 *z*	0.4861(5)	0.4858(5)	0.4859(5)	0.4861(5)	0.4861(5)	0.4857(5)	0.4860(5)	0.4855(5)	0.4861(5)	0.4852(5)	0.4854(5)	0.4852(6)
Ow1 Uiso	0.40(3)	0.35(3)	0.33(3)	0.40(3)	0.39(3)	0.43(3)	0.40(3)	0.44(3)	0.46(3)	0.50(3)	0.48(3)	0.59(3)
Ow2 *x*	0.5257(5)	0.5252(6)	0.5264(6)	0.5252(5)	0.5255(5)	0.5255(6)	0.5264(6)	0.5252(6)	0.5256(6)	0.5255(6)	0.5261(6)	0.5259(6)
Ow2 *y*	0.4464(5)	0.4463(1)	0.4464(1)	0.4465(1)	0.4464(1)	0.4464(1)	0.4465(1)	0.4464(1)	0.4463(1)	0.4463(1)	0.4461(1)	0.4461(1)
Ow2 *z*	0.0135(5)	0.0131(5)	0.0133(5)	0.0134(5)	0.0135(5)	0.0133(5)	0.0140(5)	0.01287(5)	0.0132(6)	0.0131(6)	0.0138(6)	0.0138(6)
Ow2 Uiso	0.77(3)	0.85(3)	0.85(3)	0.84(3)	0.85(3)	0.89(4)	0.94(4)	0.94(4)	1.05(4)	1.04(4)	1.16(4)	1.35(4)
D1 *x*	−0.0979(6)	−0.0981(6)	−0.0968(6)	−0.0983(6)	−0.0973(6)	−0.0979(6)	−0.0967(6)	−0.0971(6)	−0.0974(6)	−0.0979(6)	−0.0977(6)	−0.0982(7)
D1 *y*	0.3303(1)	0.3301(1)	0.3303(1)	0.3298(1)	0.3302(1)	0.3302(1)	0.3303(1)	0.3302(1)	0.3301(1)	0.3302(1)	0.3302(1)	0.3305(1)
D1 *z*	0.0346(5)	0.0338(5)	0.0348(5)	0.0338(5)	0.0349(5)	0.0342(5)	0.0349(6)	0.0342(6)	0.0343(6)	0.0337(6)	0.0344(6)	0.0338(6)
D1 Uiso	1.69(4)	1.70(4)	1.71(4)	1.73(4)	1.70(4)	1.76(4)	1.77(4)	1.77(4)	1.75(4)	1.80(4)	1.80(4)	1.84(4)
D2 *x*	0.3844(5)	0.3842(5)	0.03850(5)	0.3848(5)	0.3847(5)	0.3840(6)	0.3853(6)	0.3849(6)	0.3843(6)	0.3841(6)	0.3845(6)	0.3839(6)
D2 *y*	0.4894(1)	0.4895(1)	0.4894(1)	0.4894(1)	0.4894(1)	0.4893(1)	0.4892(1)	0.4894(1)	0.4891(1)	0.4893(1)	0.4894(1)	0.4891(1)
D2 *z*	0.4920(6)	0.4916(6)	0.4916(6)	0.4919(6)	0.4920(6)	0.4917(6)	0.4917(6)	0.4913(6)	0.4915(6)	0.4912(7)	0.4912(6)	0.4905(7)
D2 Uiso	1.39(4)	1.38(4)	1.45(4)	1.41(4)	1.43(4)	1.43(4)	1.46(4)	1.47(4)	1.47(4)	1.54(4)	1.53(4)	1.64(5)
D3 *x*	0.2050(5)	0.2055(5)	0.2062(5)	0.2058(5)	0.2057(5)	0.2061(5)	0.2065(5)	0.2064(6)	0.2061(6)	0.2054(6)	0.2062(6)	0.2058(6)
D3 *y*	0.4122(1)	0.4120(1)	0.4120(1)	0.4119(1)	0.4120(1)	0.4121(1)	0.4120(1)	0.4119(1)	0.4118(1)	0.4122(1)	0.4119(1)	0.4116(1)
D3 *z*	0.4862(6)	0.4859(6)	0.4860(6)	0.4853(6)	0.4860(6)	0.4860(6)	0.4862(6)	0.4855(6)	0.4856(6)	0.4850(6)	0.4856(6)	0.4846(6)
D3 Uiso	1.59(4)	1.57(4)	1.54(4)	1.57(4)	1.61(4)	1.58(4)	1.63(4)	1.68(4)	1.67(4)	1.72(4)	1.71(4)	1.83(5)
D4 *x*	0.5117(7)	0.5116(7)	0.5125(7)	0.5118(7)	0.5124(7)	0.5122(7)	0.5127(7)	0.5121(7)	0.5117(7)	0.5107(7)	0.5125(7)	0.5119(8)
D4 *y*	0.5107(2)	0.5107(2)	0.5106(2)	0.5108(2)	0.5107(2)	0.5108(2)	0.5108(1)	0.5109(2)	0.5109(2)	0.5107(2)	0.5104(2)	0.5106(2)
D4 *z*	0.0160(6)	0.0156(6)	0.0160(6)	0.0160(6)	0.0166(6)	0.0162(6)	0.0168(6)	0.0161(7)	0.0156(7)	0.0156(7)	0.0168(7)	0.0171(7)
D4 Uiso	2.22(5)	2.22(5)	2.30(5)	2.32(5)	2.28(5)	2.30(5)	2.31(5)	2.31(5)	2.52(5)	2.46(5)	2.47(5)	2.54(6)
D5 *x*	0.5007(6)	0.5010(6)	0.5003(6)	0.5011(6)	0.5013(6)	0.5007(6)	0.5013(6)	0.5009(6)	0.5007(6)	0.5003(6)	0.5009(6)	0.5000(7)
D5 *y*	0.4332(2)	0.4330(2)	0.4332(2)	0.4328(2)	0.4331(2)	0.4330(2)	0.4331(2)	0.4329(2)	0.4332(2)	0.4328(2)	0.4330(2)	0.4331(2)
D5 *z*	0.8546(6)	0.8543(6)	0.8541(6)	0.8543(6)	0.8552(6)	0.8548(6)	0.8550(6)	0.8539(6)	0.8549(6)	0.8540(6)	0.8551(6)	0.8548(7)
D5 Uiso	2.48(5)	2.54(5)	2.56(5)	2.49(5)	2.49(5)	2.58(5)	2.55(5)	2.68(5)	2.72(5)	2.80(5)	2.87(5)	3.03(6)

Table 4b Atomic coordinates of deuterated brushite from 150 to 400 K (Uiso values are ×100)

	150 K	175 K	200 K	225 K	250 K	275 K	300 K	325 K	350 K	375 K	400 K
Ca *x*	0.5	0.5	0.5	0.5	0.5	0.5	0.5	0.5	0.5	0.5	0.5
Ca *y*	0.3275(2)	0.3285(2)	0.3274(2)	0.3274(2)	0.3276(2)	0.3274(2)	0.3275(2)	0.3273(2)	0.3271(2)	0.3267(2)	0.3268(3)
Ca *z*	0.25	0.25	0.25	0.25	0.25	0.25	0.25	0.25	0.25	0.25	0.25
Ca Uiso	0.55(4)	0.61(4)	0.68(5)	0.72(5)	0.79(5)	0.82(6)	0.85(6)	0.81(6)	0.93(6)	1.01(7)	1.10(7)
P *x*	−0.0102(6)	−0.0096(7)	−0.0104(7)	−0.0096(7)	−0.0098(8)	−0.0082(8)	−0.0076(9)	−0.0084(9)	−0.0073(9)	−0.0053(10)	−0.0032(10)
P *y*	0.3225(1)	0.3226(1)	0.3223(1)	0.3223(2)	0.3220(2)	0.3220(2)	0.3222(2)	0.3227(2)	0.3224(2)	0.3226(2)	0.3231(2)
P *z*	0.7280(6)	0.7284(6)	0.7268(6)	0.7283(7)	0.7281(7)	0.7292(8)	0.7293(8)	0.7291(8)	0.7286(9)	0.7292(9)	0.7292(10)
P Uiso	0.11(3)	0.11(3)	0.11(3)	0.11(3)	0.13(3)	0.15(4)	0.17(4)	0.22(4)	0.23(4)	0.31(5)	0.30(5)
O1 *x*	−0.0110(6)	−0.0103(7)	−0.0102(7)	−0.0102(7)	−0.0108(8)	−0.0105(8)	−0.0102(9)	−0.0118(9)	−0.0113(9)	−0.0107(10)	−0.0109(10)
O1 *y*	0.3679(1)	0.3678(1)	0.3675(2)	0.3674(2)	0.3672(2)	0.3669(2)	0.3665(2)	0.3666(2)	0.3666(2)	0.3667(2)	0.3671(2)
O1 *z*	−0.0368(6)	−0.0371(6)	−0.0380(6)	−0.0379(7)	−0.0384(7)	−0.0391(7)	−0.0386(8)	−0.0397(8)	−0.0404(8)	−0.0420(9)	−0.0436(9)
O1 Uiso	0.57(4)	0.66(4)	0.71(4)	0.82(4)	0.89(5)	1.02(5)	1.09(6)	1.16(6)	1.20(6)	1.26(7)	1.32(7)
O2 *x*	0.2545(6)	0.2552(6)	0.2546(6)	0.2553(7)	0.2556(7)	0.2566(7)	0.2565(8)	0.2551(8)	0.2552(8)	0.2551(9)	0.2570(9)
O2 *y*	0.2818(1)	0.2818(1)	0.2818(2)	0.2818(2)	0.2821(2)	0.2817(2)	0.2819(2)	0.2818(2)	0.2821(2)	0.2817(2)	0.2812(2)
O2 *z*	0.8216(6)	0.8221(6)	0.8210(6)	0.8229(6)	0.8222(7)	0.8229(7)	0.8236(8)	0.8228(8)	0.8222(8)	0.8220(9)	0.8216(9)
O2 Uiso	0.47(3)	0.53(4)	0.63(4)	0.68(4)	0.85(5)	0.93(5)	1.08(6)	1.14(6)	1.29(6)	1.47(7)	1.66(8)
O3 *x*	−0.06319(6)	−0.0622(6)	−0.0621(7)	−0.0610(7)	−0.0606(7)	−0.0594(8)	−0.0589(8)	−0.0583(9)	−0.0578(9)	−0.0561(9)	−0.0559(10)
O3 *y*	0.3934(1)	0.3934(1)	0.3933(1)	0.3932(1)	0.3931(1)	0.3927(2)	0.3928(2)	0.3925(2)	0.3922(2)	0.3917(2)	0.3914(2)
O3 *z*	0.5413(6)	0.5412(6)	0.5407(6)	0.5417(7)	0.5407(7)	0.5413(7)	0.5415(8)	0.5405(8)	0.5409(8)	0.5404(9)	0.5398(9)
O3 Uiso	0.60(3)	0.63(4)	0.76(4)	0.86(4)	0.87(5)	0.98(5)	1.05(6)	1.20(6)	1.24(6)	1.25(7)	1.33(7)
O4 *x*	0.7780(6)	0.7786(7)	0.7785(7)	0.7782(7)	0.7777(8)	0.7778(8)	0.7781(9)	0.7774(9)	0.7783(9)	0.7797(10)	0.7810(1)
O4 *y*	0.2528(1)	0.2530(2)	0.2529(1)	0.2531(1)	0.2529(2)	0.2532(2)	0.2531(2)	0.2535(2)	0.2534(2)	0.2538(2)	0.2538(2)
O4 *z*	0.6346(6)	0.6349(6)	0.6338(6)	0.6343(7)	0.6341(7)	0.6339(8)	0.6349(8)	0.6340(8)	0.6335(9)	0.6334(9)	0.6339(9)
O4 Uiso	0.27(3)	0.33(3)	0.41(3)	0.47(4)	0.51(4)	0.60(4)	0.65(5)	0.71(5)	0.73(5)	0.78(6)	0.65(5)
Ow1 *x*	0.3653(7)	0.3653(7)	0.3656(7)	0.3650(8)	0.3654(8)	0.3655(9)	0.3658(9)	0.3640(10)	0.3640(10)	0.3631(11)	0.3620(11)
Ow1 *y*	0.4255(1)	0.4256(2)	0.4256(2)	0.4257(2)	0.4259(2)	0.4260(2)	0.4260(2)	0.4264(2)	0.4259(2)	0.4261(3)	0.4260(3)
Ow1 *z*	0.4848(6)	0.4841(6)	0.4827(6)	0.4826(7)	0.4824(7)	0.4812(8)	0.4818(8)	0.4817(9)	0.4805(9)	0.4791(10)	0.4775(10)
Ow1 Uiso	0.75(4)	0.88(4)	1.05(4)	1.21(5)	1.48(5)	1.54(6)	1.85(6)	2.03(7)	2.29(7)	2.32(8)	2.87(9)
Ow2 *x*	0.5247(7)	0.5263(7)	0.5269(7)	0.5267(8)	0.5290(8)	0.5288(9)	0.5293(9)	0.5301(10)	0.5314(10)	0.5326(11)	0.5358(11)
Ow2 *y*	0.4460(2)	0.4458(2)	0.4456(2)	0.4461(2)	0.4455(2)	0.4457(2)	0.4457(2)	0.4462(2)	0.4459(2)	0.4464(3)	0.4457(3)
Ow2 *z*	0.0134(6)	0.0149(7)	0.0153(7)	0.0163(2)	0.0182(7)	0.0191(8)	0.0208(9)	0.0217(9)	0.0228(9)	0.0232(10)	0.0259(11)
Ow2 Uiso	1.47(5)	1.58(5)	1.81(6)	1.94(6)	2.15(7)	2.44(8)	2.56(9)	2.71(9)	3.16(10)	3.61(12)	4.03(13)
D1 *x*	−0.0992(7)	−0.0977(7)	−0.0985(7)	−0.0981(8)	−0.0981(8)	−0.0982(8)	−0.0990(9)	−0.1003(9)	−0.1002(9)	−0.0992(10)	−0.1002(10)
D1 *y*	0.3303(2)	0.3303(2)	0.3300(2)	0.3299(2)	0.3300(2)	0.3299(2)	0.3300(2)	0.3300(2)	0.3308(2)	0.3316(2)	0.3315(3)
D1 *z*	0.0332(6)	0.0339(6)	0.0322(7)	0.0333(7)	0.0335(7)	0.0332(8)	0.0329(9)	0.0315(9)	0.0308(9)	0.0307(10)	0.0295(10)
D1 Uiso	1.92(5)	1.95(5)	2.01(5)	2.19(6)	2.36(6)	2.49(6)	2.70(7)	2.97(8)	3.12(8)	3.15(9)	3.40(9)
D2 *x*	0.3829(6)	0.3850(7)	0.3837(7)	0.3837(7)	0.3845(7)	0.3826(8)	0.3827(9)	0.3813(9)	0.3809(9)	0.3803(10)	0.3802(10)
D2 *y*	0.4892(2)	0.4890(2)	0.4891(2)	0.4888(2)	0.4891(2)	0.4890(2)	0.4886(2)	0.4886(2)	0.4886(2)	0.4886(3)	0.4879(3)
D2 *z*	0.4901(7)	0.4918(7)	0.4902(8)	0.4912(8)	0.4907(9)	0.4899(9)	0.4883(10)	0.4870(10)	0.4841(11)	0.4821(11)	0.4810(12)
D2 Uiso	1.66(5)	1.69(5)	1.83(5)	1.95(6)	2.01(6)	2.07(6)	2.36(7)	2.59(7)	2.66(8)	2.80(8)	3.40(9)
D3 *x*	0.2053(6)	0.2061(6)	0.2067(7)	0.2057(7)	0.2067(7)	0.2054(8)	0.2056(8)	0.2047(8)	0.2050(9)	0.2046(9)	0.2042(10)
D3 *y*	0.4117(1)	0.4118(2)	0.4117(2)	0.4118(2)	0.4119(2)	0.4119(2)	0.4119(2)	0.4123(2)	0.4125(2)	0.4120(2)	0.4119(2)
D3 *z*	0.4843(6)	0.4845(7)	0.4832(7)	0.4823(7)	0.4816(8)	0.4794(8)	0.4781(8)	0.4772(9)	0.4766(9)	0.4743(9)	0.4744(10)
D3 Uiso	1.97(5)	2.12(5)	2.27(6)	2.31(6)	2.62(7)	2.69(7)	2.84(8)	2.93(8)	2.91(8)	2.90(9)	3.30(10)
D4 *x*	0.5112(8)	0.5140(8)	0.5154(9)	0.5149(9)	0.5186(10)	0.5188(10)	0.5216(11)	0.5190(12)	0.5233(13)	0.5260(14)	0.5305(15)
D4 *y*	0.5106(2)	0.5105(2)	0.5103(2)	0.5105(2)	0.5102(2)	0.5103(3)	0.5099(3)	0.5096(3)	0.5090(4)	0.5080(4)	0.5074(5)
D4 *z*	0.0171(7)	0.0181(8)	0.0171(8)	0.0191(9)	0.0203(9)	0.0211(10)	0.0219(11)	0.0203(12)	0.0199(13)	0.0217(14)	0.0236(16)
D4 Uiso	2.81(6)	3.02(7)	3.29(7)	3.59(8)	4.09(9)	4.62(10)	5.24(11)	6.41(14)	7.36(15)	8.36(18)	9.46(20)
D5 *x*	0.5006(7)	0.5024(7)	0.5032(8)	0.5038(8)	0.5055(9)	0.5070(10)	0.5085(10)	0.5072(11)	0.5070(12)	0.5077(12)	0.5087(13)
D5 *y*	0.4332(2)	0.4328(2)	0.4329(2)	0.4331(2)	0.4332(3)	0.4335(3)	0.4338(3)	0.4343(3)	0.4343(4)	0.4348(4)	0.4357(4)
D5 *z*	0.8561(7)	0.8584(7)	0.8576(8)	0.8608(8)	0.8630(8)	0.8655(9)	0.8677(10)	0.8683(10)	0.8688(10)	0.8702(11)	0.8732(12)
D5 Uiso	3.34(6)	3.50(7)	3.93(7)	4.27(8)	4.73(9)	5.09(10)	5.51(11)	6.11(13)	6.75(14)	7.09(15)	7.90(17)

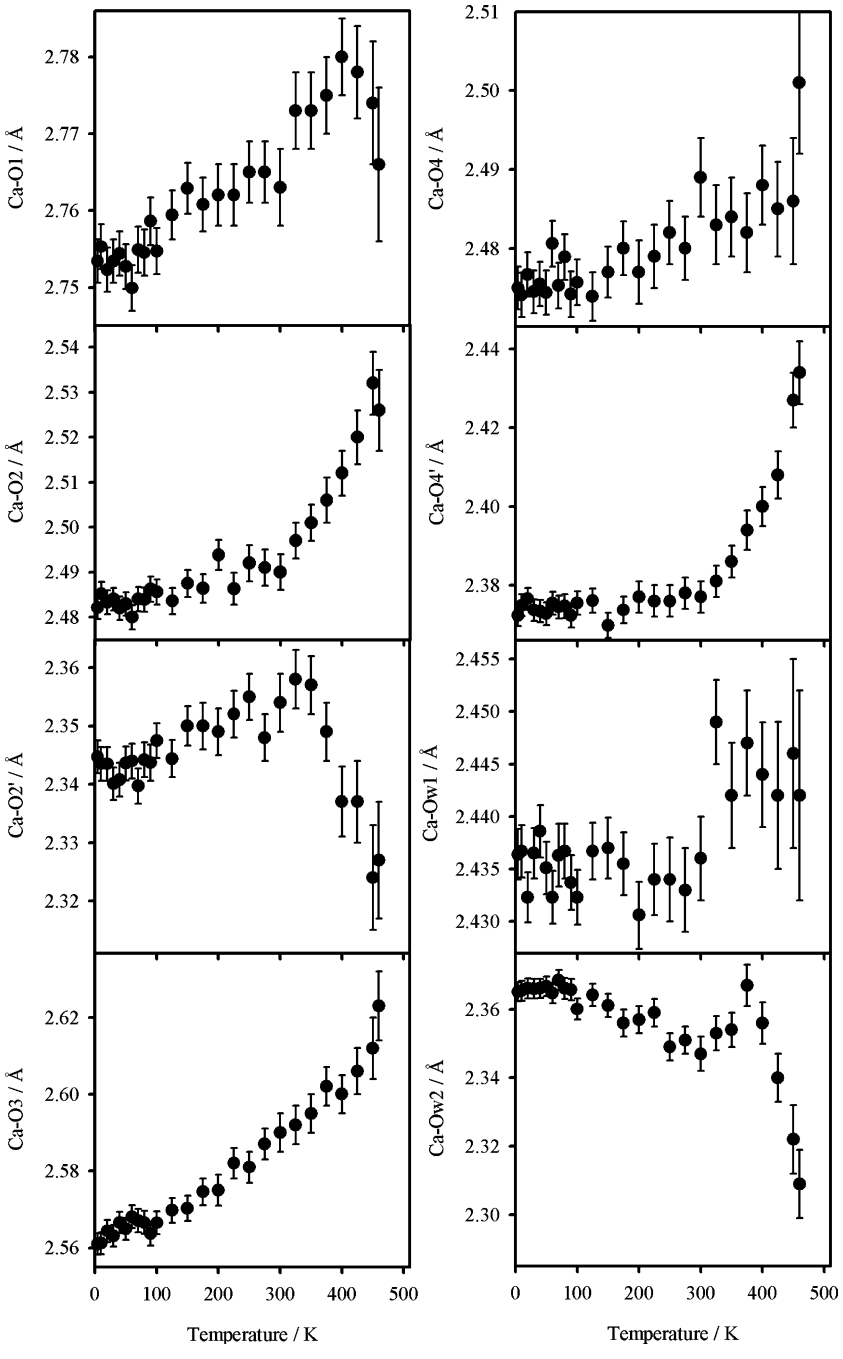

Fig. 4 The variation of the Ca–O bond lengths within the polyhedral sheets of deuterated brushite as a function of temperature in the range $4.2 \leq T \leq 460$ K

The combined effect of these changes results in a gradual increase in the volume of the PO_4 tetahedra until about 275–300 K, where the volume suddenly decreases rapidly, and a tendency towards a more regular geometry with the quadratic elongation decreasing slowly as a function of temperature until about 275–300 K, where it also decreases sharply (Fig. 7). The O1-D bond of the acidic proton associated with the PO_4 group remains relatively constant up to about 100 K above which it increases up to about 300 K and then decreases again (Fig. 8). The short hydrogen bond D1···O4 shows no such anomalous behaviour and increases as a function of increasing temperature. The rate of this hydrogen bond lengthening increases significantly above 300 K. The hydrogen bond angle O1–D1···O4 shows a slight decrease up to about 275–300 K, above which the decrease becomes much larger.

The water molecules in brushite are asymmetric, non-equivalent and significantly distorted from those of a free water molecule and, as may be expected, their temperature-dependent behaviours are slightly different from each other. All the intramolecular O–D bonds decrease as a function of increasing temperature (Fig. 9) with Ow1-D3 and Ow2-D5 decreasing almost linearly

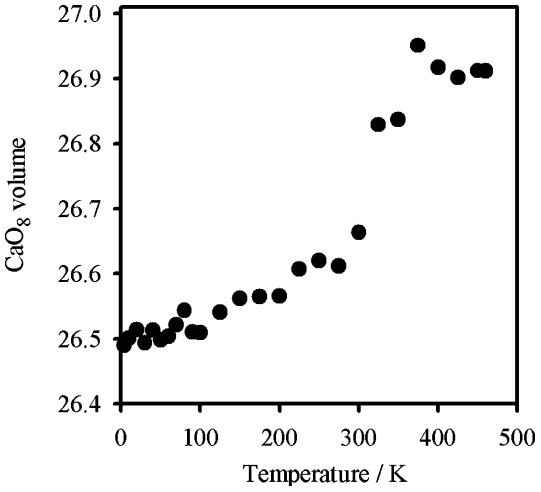

Fig. 5 Volume of the CaO_8 polyhedra as a function of temperature

across the temperature range by 2.0% (0.0304 Å) and 4.0% (0.0380 Å), respectively. Ow1-D2 shows no temperature-dependent change below about 100 K, but above this decreases more rapidly, with an overall shortening of 2.0% (0.0191 Å) and Ow2-D4 showing no change until about 300 K, where the bond shortens by 3.8% (0.0373 Å) in the next 100 K. The D2–Ow1–D3 angle of the first water molecule becomes more distorted as temperature increases widening by 2° to a value above 109°, whereas the D4–Ow2–D5 angle of the second water molecule shows no change until about 250–275 K, above which it apparently decreases by up to 5° reaching about 99° at 400 K.

The hydrogen bonds associated with the second water molecule appear to vary more than those of the first water molecule (Fig. 10). The D5···Ow1 and D4···O1 hydrogen bonds increase by almost 9% (0.1824 Å) and 5% (0.0881 Å), respectively, whereas the D2···O3 bond increases by about 4% (0.0769 Å), but the D3···O3 bond, which shows very little change as a function of temperature, actually decreases slightly by about 0.4% (0.0062 Å). The hydrogen bonds associated with the second water molecule remain relatively unchanged up to about 150 K, while the D2···O3 hydrogen bond increases slightly up to about 200 K, above which the rate of bond lengthening increases significantly. Although varying little, D3···O3 appears to have an oscillatory behaviour, with a final decrease beginning at about 300 K. The angles of both of the hydrogen bonds associated with the second water molecule (Ow2–D4···O1 and Ow2–D5···Ow1) show a slight decrease before increasing rapidly from about 275–300 K, whereas the equivalent angles for the hydrogen bonds of the first water molecule (Ow1–D2···O3 and Ow1–D3···O3) both show an overall decrease, with Ow1–D2···O3 increasing slightly up to about 275–300 K before decreasing and Ow1–D3···O3 appearing to have reached a distortion limit or minimum at about 300 K.

The asymmetry of the hydrogen bonds is a good indicator of their relative straining and strength (i. e. weak or strong) and the temperature-dependent variation of the interanion distances of the hydrogen bonding in brushite is shown in Fig. 11. The interanion distance O1···O4 associated with the hydrogen bonding of the HPO_4^{2-} groups shows the smallest variation in distance (2.668 Å–2.699 Å) and angle (167.3°–164.5°) as temperature is increased, and remains the strongest hydrogen bond within the structure throughout the temperature range. The Ow1···O3(D3) hydrogen bond also remains relatively strong by comparison with the three remaining hydrogen bonds, decreasing from 2.723 Å at 4.2 K to 2.680 Å at 400 K although the angle decreases from 169.7° to 166.6°. The Ow1···O3(D2) and Ow2···O1 hydrogen bonds are significantly weaker and show larger increases than O1···O4 and Ow1···O(D2), with increases on the order of 0.05 Å across the temperature range. Ow1···O3(D2) increases from 2.763 to 2.817 Å with a simultaneous decrease in angle from 173.1° to 171.0°, while Ow2···O1 increases from 2.823 to 2.876 Å accompanied by a slight increase in angle from 168.9° to 169.6°. The weakest of the hydrogen bonds is Ow2 ···Ow1, increasing by 0.15 Å from 2.986 Å at 4.2 K to 3.136 Å at 400 K, with a bond-angle increase from 165.4° to 167.7°, approaching the maximum limit for donor–acceptor distances (Baur, 1972; Brown, 1976).

Brushite is essentially a layered structure with layers, comprising SO_4^{2-} units and CaO_8 polyhedra, parallel to the (010) face being weakly bound together by a layer of H_2O molecules. In this respect, it may be expected that the response of the water molecules to increasing temperature will depict the nature of the thermal expansion of brushite. Indeed, the hydrogen bonds D2···O3 and D4···O1 act predominantly along *b*, and with increases on the order of 0.077 and 0.088 Å, respectively, are clearly the dominant influence on the expansion of the *b* lattice parameter. The thermal expansion of gypsum is quite strongly anisotropic, with the expansion along *b* almost three times larger than that along *c* (Schofield et al. 1996); however, in brushite the expansion along *c* is only about 10% less than that along *b*. In the brushite structure a large component of the D5···Ow1 hydrogen bond acts along *c,* and as this bond displays the largest expansion of any of the bonds, expanding by 0.182 Å (an increase of almost 9%), there is larger than expected thermal expansion of the unit cell in that direction. In a nature analogous to that of gypsum, the hydrogen bond with an effectively zero thermal expansion, D3···O3, acts primarily along *a*, the axis with the lowest overall thermal expansion. The significance of these hydrogen bonds upon the thermal expansion of brushite is further highlighted when compared with the orientation of the thermal expansion tensor, with the maximum, intermediate and minimum principal axes (α_{11}, α_{22} and α_{33}) being parallel to the D5···Ow1, D2···O3 / D4···O1, and the D3···O3 hydrogen bonds, respectively.

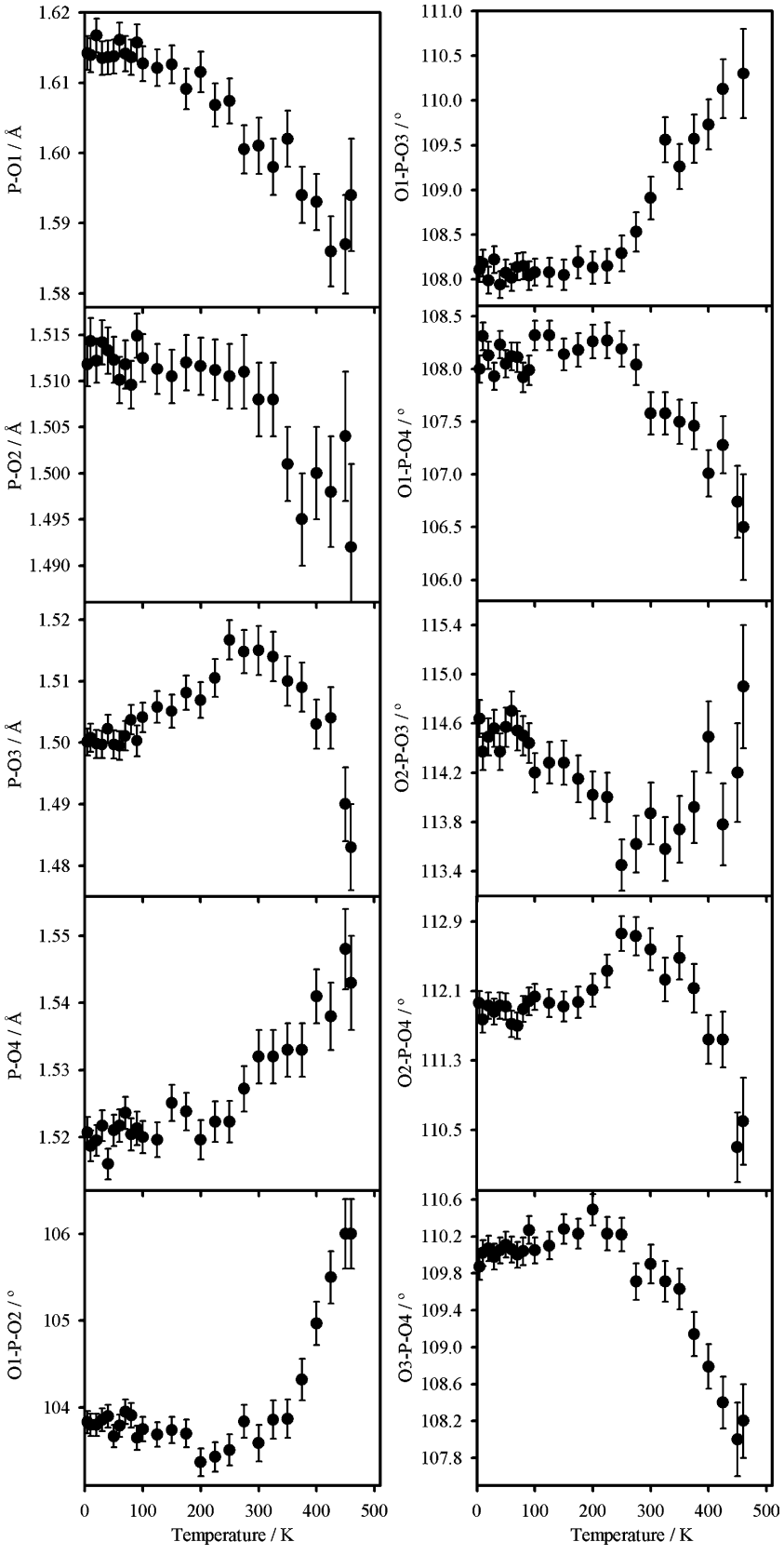

Fig. 6 The variation of the bond lengths and angles within the PO_4 tetrahedra of deuterated brushite as a function of temperature in the range $4.2 \leq T \leq 460$ K

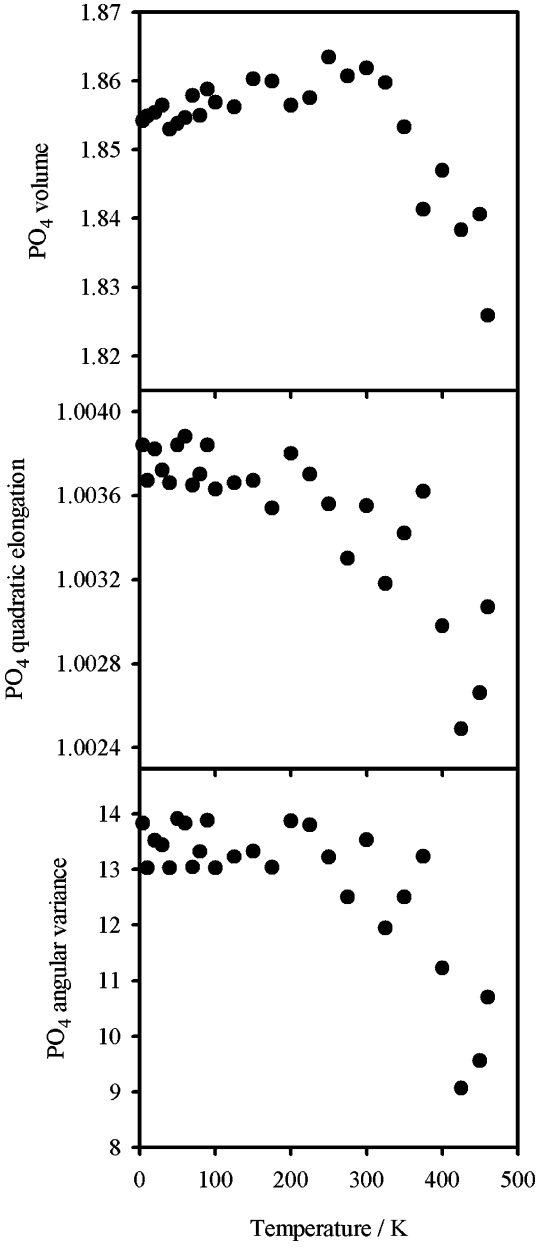

Fig. 7 Volume and quadratic elongation of the PO_4 tetrahedra as a function of temperature

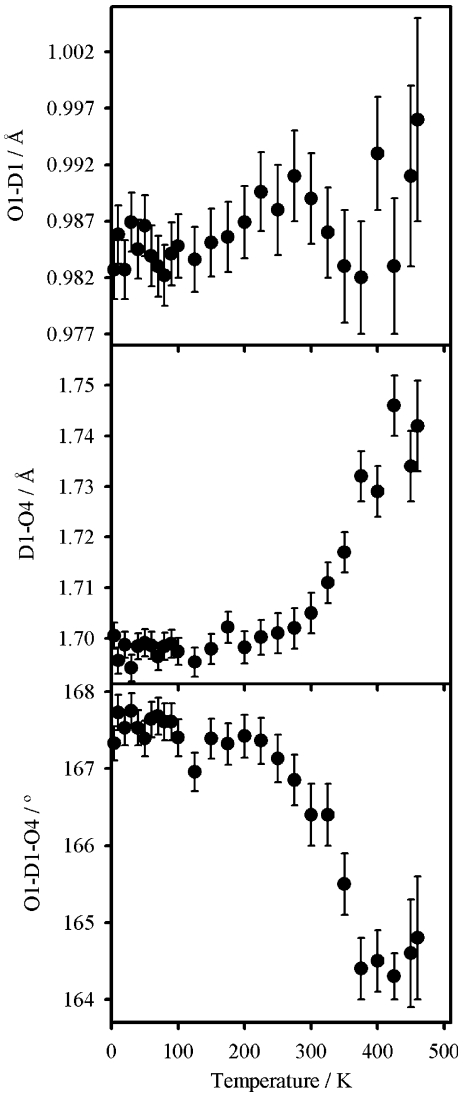

Fig. 8 Temperature dependence of the O–D and hydrogen bond lengths and the hydrogen bond angle of the acidic D atom in brushite between 4.2 and 460 K

Dehydration

We first observed evidence, albeit subtle, for dehydration products at 425 K, which agrees well with the temperature range of 150–180 °C determined by McIntosh and Jablonski (1956). As a consequence, modelling and discussion of the thermal expansion of brushite was limited to the temperature range 4.2 to 400 K, although structural refinements of the brushite structure were performed on data up to 460 K. Significant dehydration was not observed until 470 K, whereby the data were such that only cell refinements could be performed on the diffraction data, and from Fig. 2 it appears that the unit-cell volume also appears to be saturating at this temperature.

The *a* parameter saturates at about 400 K, perhaps reflecting the saturation of the Ow1–D3 bond and the decrease in the D3···O3 hydrogen bond which act primarily in this direction. As the polyhedral layers of the brushite structure comprise zig-zag chains of CaO_8 and PO_4 polyhedra running parallel to *a,* it seems likely that these polyhedral layers will impart a significant influence on the behaviour of the structure in this direction. Indeed, Fig. 5 shows that the volume of the CaO_8 polyhedra has saturated at 400 K, perhaps reflecting the decrease or saturation of the Ca–O1, Ca–Ow1 and Ca–Ow2 bonds at 400 K. The *b* and *c* cell edges, on the other hand, continue to expand up to about 470 K, at which point dehydration is well under way. This seems to

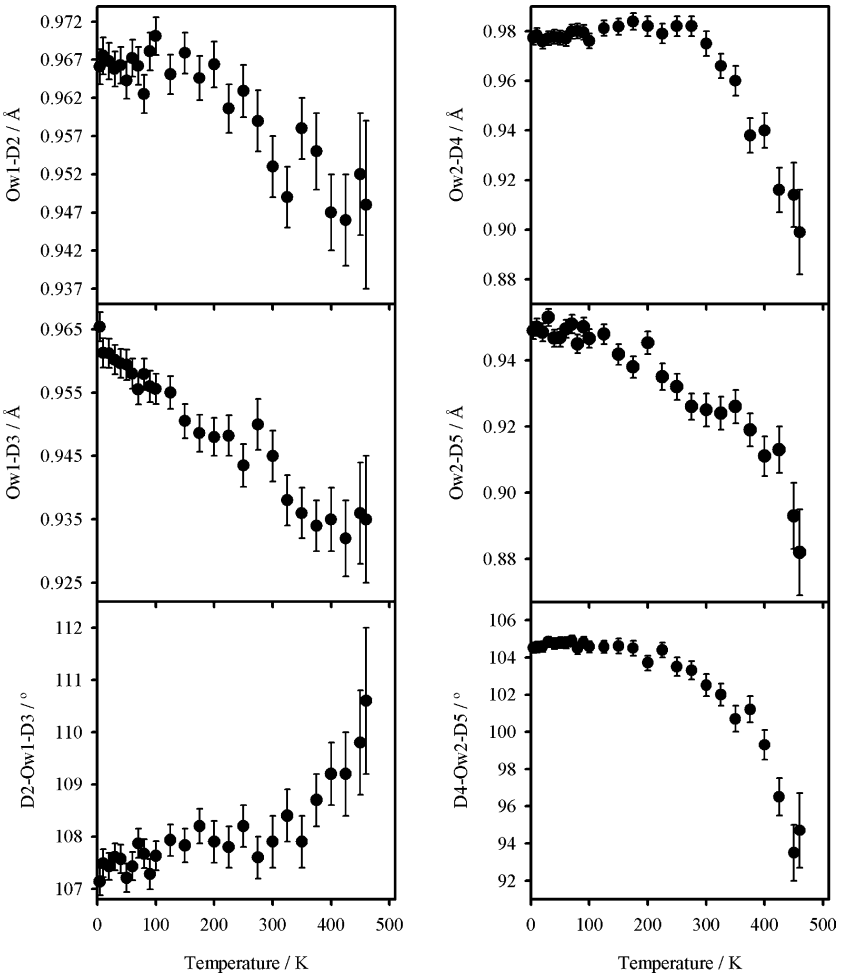

Fig. 9 The variation of the D–O bond lengths and the D–O–D bond angles of the water molecules of deuterated brushite in the temperature range $4.2 \leq T \leq 460$ K

reflect the behaviour of the D2···O3, D4···O1 and the D5···Ow1 hydrogen bonds (Fig. 10), which seem to keep expanding up to 460 K.

As the acidic proton of the HPO_4^{2-} groups in brushite are also present in monetite, albeit disordered across two sites (Catti et al. 1977, 1980), it seems probable that it has a minimal role in the dehydration mechanism of brushite to monetite. By contrast, as an absolute minimum, the hydrogen bonding associated with the water molecules must be broken. As already established the Ow2···Ow1 interanion distance is by far the largest and by 460 K has reached over 3.2 Å (Fig. 11), with the hydrogen bond D5···Ow1 expanding to over 2.3 Å and the Ow2-D5···Ow1 angle approaching linearity (Fig. 10). The second hydrogen bond associated with Ow2 is through D4, with the interanion distance Ow2···O1 expanding rapidly towards 3 Å (Fig. 11) but has potentially reached its maximum limit at about 450 K. The D4···O1 hydrogen bond has expanded above 2.0 Å and it may be that the hydrogen bond angle Ow2-D5···Ow1 has reached a maximum close to linearity (Fig. 10), with the distortion of the intrawater angle reaching a limit at about 93° (Fig. 9). This water molecule has become highly strained and distorted with the hydrogen bonding becoming progressively weaker and, as these bonds weaken, the hydrogen atoms should be able to vibrate much more freely. This is borne out by the thermal parameters for D4 and D5 (Table 4), which are significantly larger than those for any other of the hydrogen atoms and have increased in magnitude by four and three times, respectively. The thermal parameter for Ow2 (Table 4) has increased in magnitude between five and six times while the Ca–Ow2 bond, that has maintained a fairly consistent length across most of the temperature range, suddenly begins to decrease rapidly at about 400 K, becoming the shortest bond within the CaO_8 polyhedron (Fig. 4).

The first water molecule shows behaviour slightly different to that of the second water molecule as dehydration is approached. The hydrogen bond associated with D3 becomes increasingly strained, especially above 400 K, with the interanion distance Ow1-O3(D3) decreasing towards 2.6 Å (Fig. 11), and the hydrogen bond length D3···O3 and the hydrogen bond angle Ow1-D3···O3 both also decreasing rapidly (Fig. 10). The D2···O3 hydrogen bond has increased to over 1.9 Å at 460 K while the Ow1–D2···O3 hydrogen bond angle decreases further above 400 K despite appearing

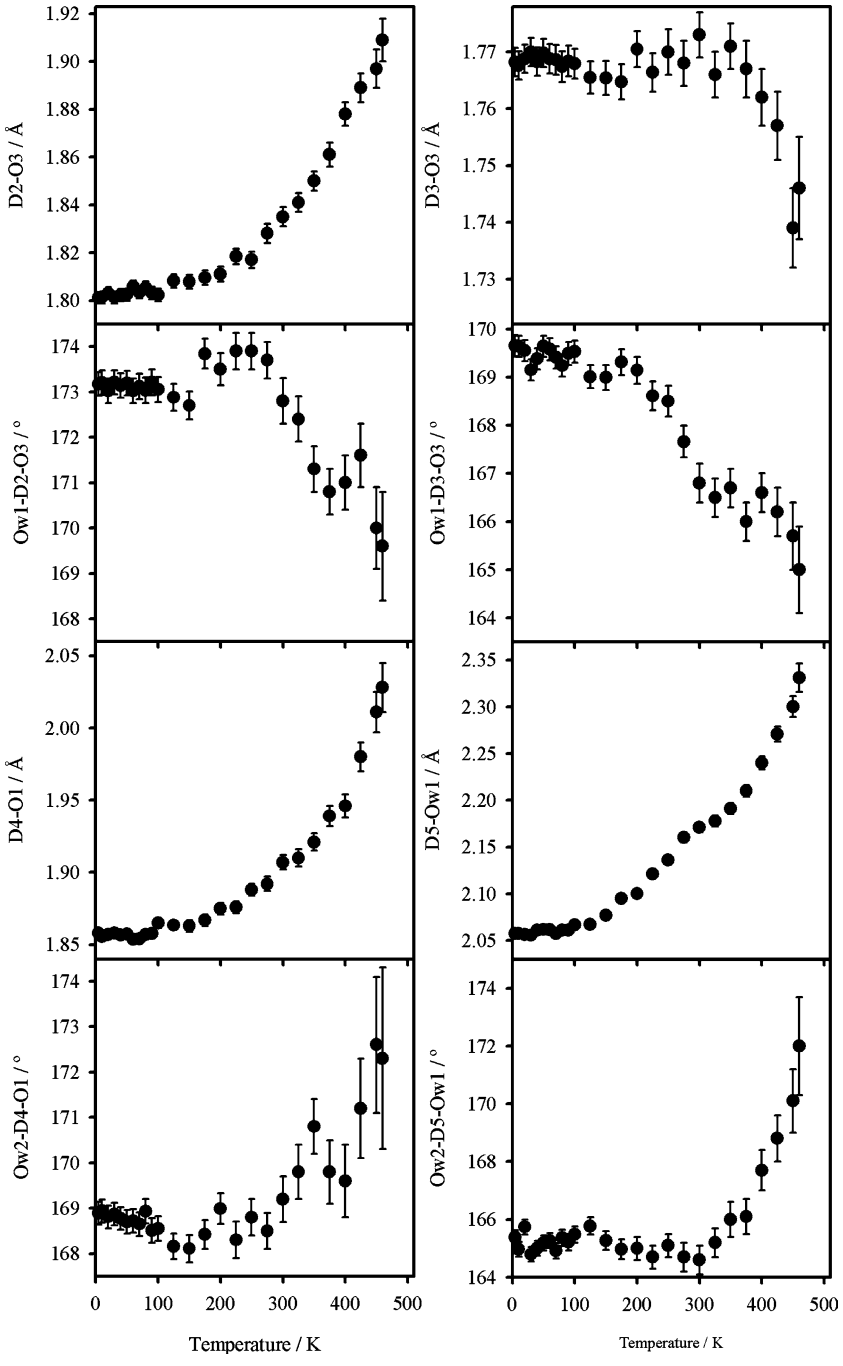

Fig. 10 Temperature dependence of the hydrogen bond lengths and angles of deuterated associated with the water molecules of brushite in the range $4.2 \leq T \leq 460$ K

to be saturated prior to this temperature (Fig. 10). At 460 K the intrawater angle of the first water molecule has increased above 110° and, by comparison to the thermal parameters of the hydrogen atoms of the second water molecule, those of the hydrogen atoms of the first water molecule have only doubled in magnitude (Table 4). In contrast to this, the thermal parameter of Ow1 has increased in magnitude by about seven times (Table 4), and the Ca–Ow1 bond length (Fig. 4) shows no increase above about 300 K.

Bond valence analysis is another approach that may be able to provide corroborative evidence to that of the analysis of the bond lengths and angles presented up until now. With a view to isolating potential instabilities within the expanding brushite structure, we used the parameters of Brown and Altermatt (1985) and at http://www.ccp14.ac.uk/ccp/web-mirrors/i_d_brown (Table 5) to calculate the nominal valencies on the individual ions within the brushite structure as a function of temperature, and these are presented in Figs. 12 and 13. While the nominal charge on the acidic D1 decreases towards a classical value of 1.0, those of D3, D4 and D5 all increase rapidly towards 1.2, 20% above the expected value. The nominal valence on Ow1 increases towards

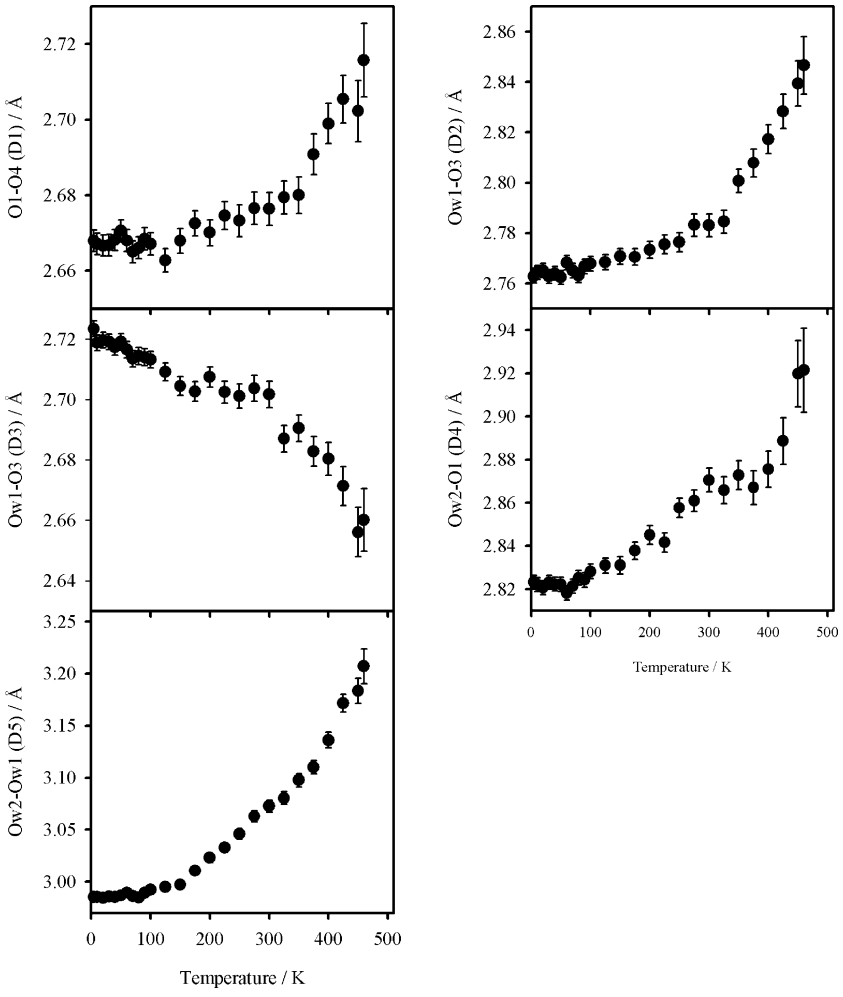

Fig. 11 Variation of the R_{OO} interanion distances of the hydrogen bonds in brushite as a function of temperature

2.2, while that of Ow2 increases upwards of 2.5. While the formal valences of the remaining ions do vary as a function of temperature, it is generally either towards a value representative of a more stable bonding environment, or to values that remain within reasonable limits of the structure.

Table 5 Empirical bond valence values (valence units) for brushite at 300 K calculated using the structural data from this study and the curves of Brown and Altermatt (1985) and http://www.ccp14.ac.uk/ccp/web-mirrors/i_d_brown

	Ca	P	D1	D2	D3	D4	D5	Total
O1	0.12	1.04	0.75			0.21		2.12
O2	0.24	1.34						1.59
O2′	0.35							0.35
O3	0.19	1.32		0.24	0.27			2.01
O4	0.24	1.26	0.30					1.80
O4′	0.33							0.33
Ow1	0.28			0.85	0.87		0.14	2.14
Ow2	0.36					0.78	0.94	2.08
Total	2.11	4.96	1.04	1.09	1.14	1.00	1.07	
O1	0.12	1.04	0.75			0.21		2.12
O2	0.59	1.34						1.94
O3	0.19	1.32		0.24	0.27			2.01
O4	0.57	1.26	0.30					2.13
Ow1	0.28			0.85	0.87		0.14	2.14
Ow2	0.36					0.78	0.94	2.08
Total	2.11	4.96	1.04	1.09	1.14	1.00	1.07	

Taking into account both of these two approaches, it does seem likely that the chemical environments associated with the atoms of the two water molecules are very unstable. While the hydrogen bonding of the first water molecule becomes increasingly strained, that of the second water molecule becomes increasingly weak. Indeed, bond valence analysis suggests that the nominal bond valence of the Ow2–D5 intrawater molecule bond becomes ten times larger than that of the corresponding D5···Ow1 hydrogen bond. The evidence from this work seems to suggest that it is an instability associated with the second water molecule that brings on the onset of dehydration, the ramifications of which may instantly cause bond breaking associated with the first water molecule, whose chemical environment is already strained and unstable.

Assessment of the bond length, bond angle and polyhedral data in Figs. 4–11 and the empirical bond valence values in Figs. 12 and 13 shows that there is a distinct change in the behaviour of the brushite structure at about 300 K. These changes are observed by a

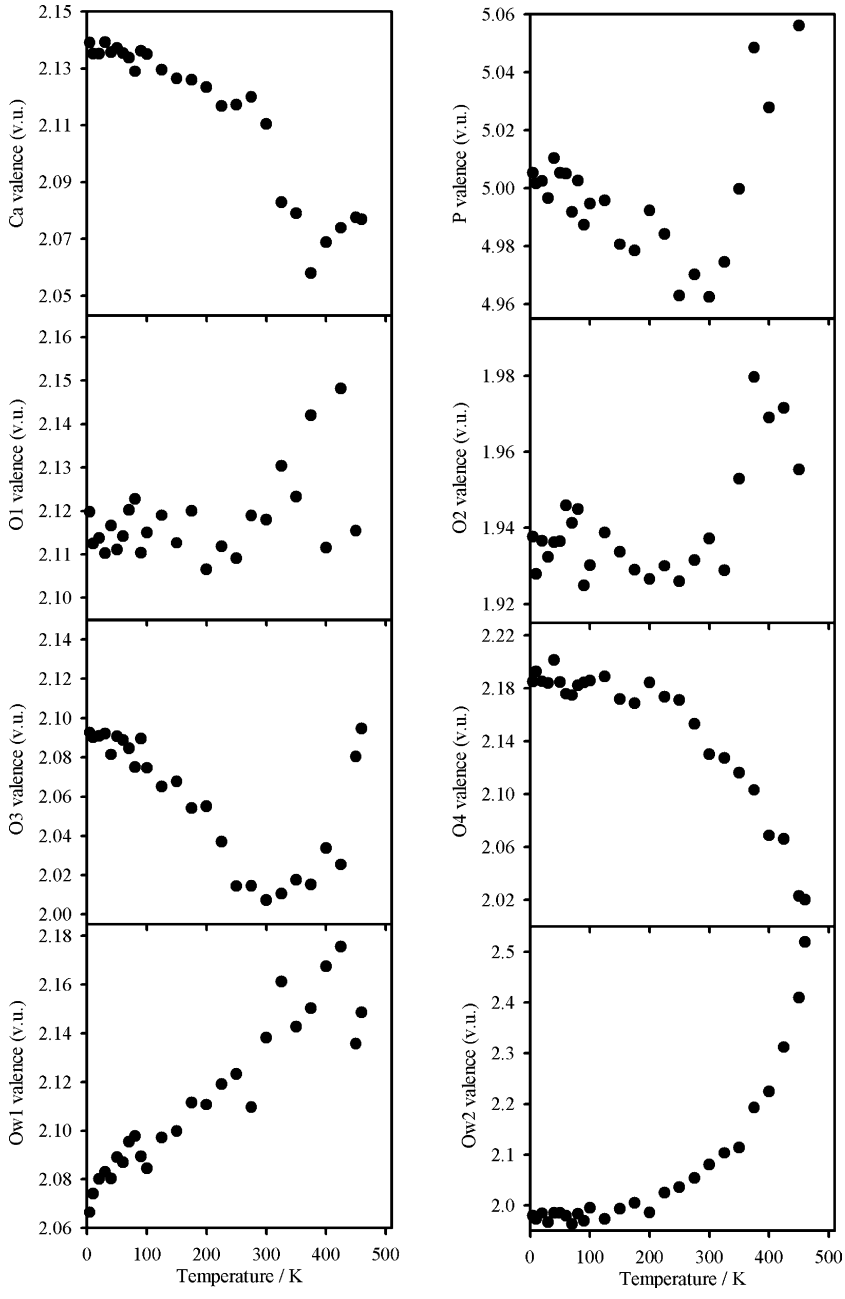

Fig. 12 Empirical bond valence values (valence units) for the Ca, P and O atoms in deuterated brushite as a function of increasing temperature from 4.2 to 460 K. These values have been calculated using the structural data from this study and the curves of Brown and Altermatt (1985) and http://www.ccp14.ac.uk/ccp/web-mirrors/i_d_brown

sudden increase in the rate of change, a distinct perturbation in the temperature-dependent trend of the data or by a total reversal in the nature of the temperature-dependent variation of the data. While changes in the trends of some of the data that occur at about 400 K are also evident in the lattice parameter data of Fig. 2, the changes evident in most of the data at about 300 K are evident only in the β-angle data of Fig. 2. It may be that at about 300 K there is a change in the driving force behind the temperature-dependent response of the brushite structure, perhaps changing from a standard thermal expansion response to a drive towards dehydration. The fact that this change in behaviour is observed very strongly in the empirical bond valence values suggests that the limits for electrostatically stable structure have been reached at about 300 K.

Conclusions

The thermal expansion of brushite is anisotropic, with the expansion along *b* and *c* being far greater than that along *a,* and seems to be related to the hydrogen bonding associated with the structurally bound water molecules. Above 400 K the crystal structure of brushite has reached the limits of its stability and begins to dehydrate, a process that may be related to an instability in the chemical environment around the water molecules. It is possible that the second water molecule be-

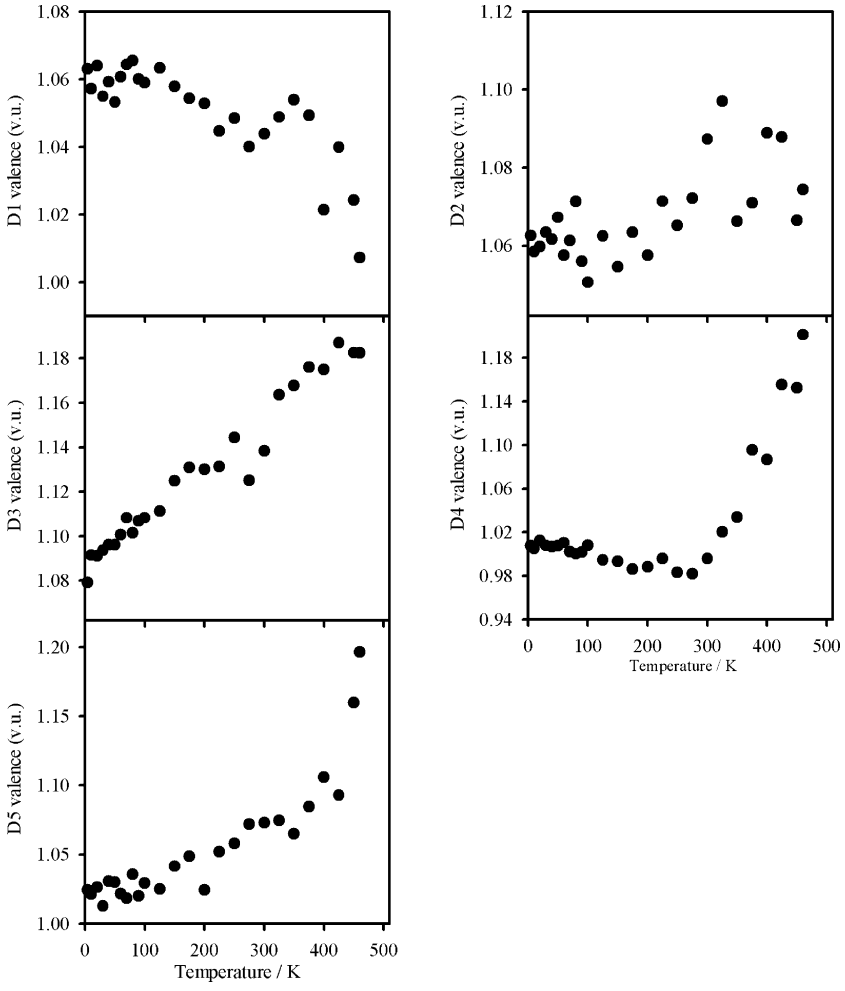

Fig. 13 Empirical bond valence values (valence units) for the D atoms in deuterated brushite as a function of increasing temperature from 4.2 to 460 K. These values have been calculated using the structural data from this study and the curves of Brown and Altermatt (1985) and http://www.ccp14.ac.uk/ccp/web-mirrors/i_d_brown

comes unstable just prior to the first water molecule, but the removal of both molecules causes the structural collapse, producing the triclinic anhydrous dicalcium phosphate monetite, in which the acidic proton of the HPO_4 groups is structurally disordered.

Acknowledgements The authors acknowledge beamtime grant from ISIS, and funding of JAMVDH's PhD studentship by CEEP (Centre Européen d' Etudes des Polyphosphates, a sector group of CEFIC, the European Chemical Industry Council).

References

Abbona F, Franchini-Angela M (1990) Crystallization of calcium and magnesium phosphates from solutions of low concentration. J Cryst Growth 104: 661–671

Baur WH (1972) Prediction of hydrogen bonds and hydrogen atoms positions in crystalline solids. Acta Crystallogr B28: 1456–1465

Beevers CA (1958) The crystal structure of dicalcium phosphate dihydrate, $CaHPO_4.2H_2O$. Acta Crystallogr 11: 273–277

Berry EE, Baddiel CB (1967) The infra-red spectrum of dicalcium phosphate dihydrate (brushite). Spectrochim Acta 23A: 2089–2097

Brown ID, Altermatt D (1985) Bond valence parameters obtained from a systematic analysis of the Inorganic Crystal Structure Database. Acta Crystallogr B41: 244–247

Brown ID (1976) On the geometry of O-H···O hydrogen bonds. Acta Crystallogr B32: 24–31

Catti M, Ferraris G, Filhol A (1977) Hydrogen bonding in the crystalline state. $CaHPO_4$ (monetite), $P\bar{1}$ or P1? A novel neutron diffraction study. Acta Crystallogr B33: 1223–1229

Catti M, Ferraris G, Mason SA (1980) Low-temperature ordering of hydrogen atoms in $CaHPO_4$ (monetite): X-ray and neutron diffraction study at 145 K. Acta Crystallogr B36: 254–259

Curry NA, Jones DW (1971) Crystal structure of brushite, calcium hydrogen orthophosphate dihydrate: a neutron diffraction investigation. J Chem Soc A: Inorg Phys Theor 3725–3729

Elliott JC (1994) Structure and chemistry of the apatites and other calcium orthophosphates. Studies in Inorganic Chemistry Vol 18. Elsevier Amsterdam-London-New York-Tokyo, pp389

Farmer VC (1974) The infrared spectra of minerals. Mineralogical Society, London.

Ferraris G (1969) The crystal structure of pharmacolite, $CaHAsO_4.2H_2O$. Acta Crystallogr B25: 1544–1550

Ferraris G, Jones DW, Yerkees J (1971) Determination of hydrogen positions in the crystal structure of pharmacolite, $CaHAsO_4.2H_2O$, by neutron diffraction. Acta Crystallogr B27: 349–354

Francis MD, Webb NC (1971) Hydroxyapatite formation from hydrated calcium monohydrogen phosphate precursor. Calc Tiss Research 6: 335–342

Fiore S, Laviano R (1991) Brushite, hydroxylapatite, and taranakite from apulian caves (southern Italy)—new mineralogical data. Amer Mineral 76: 1722–1727

Fixen PE, Ludwick AE, Olsen SR (1983) Phosphorus and potassium fertilisation of irrigated alfalfa on calcareous soils: II Soil phosphorus solubility relationships. Soil Sci Soc Am J 47: 112–117

Jessen SM, Kuppers H (1991) The precision of thermal expansion tensors of triclinic and monoclinic crystals. J Appl Crystallogr 24: 239–242

Jones DW, Smith JAS (1960) Proton magnetic resonance in brushite. Trans Faraday Soc 56: 638–647

Jones DW, Smith JAS (1962) The structure of brushite, $CaHPO_4.2H_2O$. J Chem Soc 1414–1420

Knight KS (1996) A neutron powder diffraction determination of the thermal expansion tensor of crocoite ($PbCrO_4$) between 60 K and 290 K. Mineral Mag 60: 963–972

Knight KS, Stretton IC, Schofield PF (1999) Temperature evolution between 50 K and 320 K of the thermal expansion tensor of gypsum derived from neutron powder diffraction data. Phys Chem Minerals 26: 477–483

Koutsoukos PG (1998) Influence of metal ions on the crystal growth of calcium phosphates. In: Amjad Z (ed) Calcium phosphates in biological and industrial systems. Kluwer Academic Publishers, Massachusetts, pp 145–171

Larson AC, Von Dreele RB (1994) General Structure Analysis System (GSAS), Los Alamos National Laboratory Rept. LAUR 86–748 (revised version)

McIntosh AO, Jablonski WL (1956) X-ray powder patterns of the calcium phosphates. Analytical Chem 28: 1424–1427

Nriagu JO (1984) Phosphate minerals: their properties and general modes of occurrence. In: Nriagu JO, Moore PB (eds) Phosphate minerals. Springer, Berlin Heidelberg New York, pp 1–136

Onac BP, Mylroie JE, White WB (2001) Mineralogy of cave deposits on San Salvador Island, Bahamas. Carbon Evap 16: 8–16

Pedersen BF, Semmingsen D (1982) Neutron diffraction refinement of the structure of gypsum. $CaSO_4{\cdot}2H_2O$. Acta Crystallogr B38: 1074–1077

Petrov I, Šoptrajanov B, Fuson N, Lawson JR (1967). Infra-red investigation of dicalcium phosphates. Spectrochim Acta 23A: 2637–2646

Roufosse AH, Landis WJ, Sabine WK, Glimcher MJ (1979) Identification of brushite in newly deposited bone mineral from embryonic chicks. J Ultrastuct Res 68: 235–255

Sainz-Díaz CI, Villacampa A, Otálora F (2004) Crystallographic properties of the calcium phosphate mineral, brushite, by means of first principles calculations. Am Mineral 89: 307–313

Schlenker JL, Gibbs, GV, Boison MB (1975) Thermal expansion coefficients for monoclinic crystals: A phenomonological approach. Amer Mineral 60: 823–833

Schofield PF, Knight KS, Stretton IC (1996) Thermal expansion of gypsum investigated by neutron powder diffraction. Amer Mineral 81: 847

Sears VF (1992) Neutron scattering lengths and cross sections. Neutron News 3: 26–37

Smith RI, Hull S, Armstrong AR (1994) The POLARIS powder diffractometer at ISIS. Mat Sci Forum 166–169: 251–256

Tortet L, Gavarri JR, Nihoul G. Dianoux AJ (1997) Study of protonic mobility in $CaHPO_4{\cdot}2H_2O$ (brushite) and $CaHPO_4$ (monetite) by infrared spectroscopy and neutron scattering. J Solid State Chemistry 132: 6–16

Tortet L, Gavarri JR, Musson J, Nihoul G. Sarychev AK (1998) Percolation and modeling of proton conduction in polymer/brushite composites. J Solid State Chemistry 141: 392–403

Valsami-Jones E (2001) Mineralogical controls on phosphorous recovery from wastewaters. Mineral Mag 65: 611–620

Wikholm NW, Beebe RA, Kittelberger JS (1975) Kinetics of the conversion of monetite to calcium pyrophosphate. J Phys Chem 79: 853–856

Wilson CC (1995) A guided tour of ISIS-the UK neutron spallation source. Neutron News 6: 27–34